

# Kinematic reconstruction of the Bolivian orocline

Nathan Eichelberger<sup>1,\*</sup> and Nadine McQuarrie<sup>2</sup>

<sup>1</sup>*Department of Geosciences, Princeton University, Princeton, New Jersey 08544, USA*

<sup>2</sup>*Department of Geology and Planetary Science, University of Pittsburgh, Pittsburgh, Pennsylvania 15260, USA*

## ABSTRACT

Orogenic curvature is a common feature in many mountain belts and is strongly linked to the magnitude, direction, and mechanics of crustal shortening. Determining how formation of the Bolivian orocline influenced crustal deformation in the central Andes has direct implications for geodynamics of the high-elevation Altiplano plateau. This study presents new reconstructions of the Bolivian orocline constrained by shortening estimates, thermochronology, regional paleomagnetic data, and strain data from lat 12°S to 22°S. The reconstructions investigate paleomagnetically permissible orocline limb rotations of 0°, 6°, and 13° on the kinematic compatibility of shortening constraints. Deformation was restored in 5 m.y. steps from 50 to 0 Ma, and kinematic compatibility was quantified based on the area of map-view overlap at each step. No limb rotation resulted in 14,000 km<sup>2</sup> of overlap, while 13° limb rotations and 50 km of orogen-parallel displacement on known strike-slip faults reduce overlap to 3000 km<sup>2</sup>. The preferred model builds on these results by imposing additional rotations at the orocline core and displacement on the Cochabamba fault. This model reduces overlap to 1600 km<sup>2</sup> but predicts map-view shortening estimates 70–90 km greater in the northern limb and 20–30 km greater in the southern limb than determined from cross sections. Of the modeled increase, ~20 km is due to limb rotation, while the remaining 50–70 km is due to transpressional shortening on the Cochabamba and Rio Novillero faults. Total shortening in the preferred model is 370 km in the northern limb, 380 km at the orocline core, and 300–350 in the southern limb.

## INTRODUCTION

Determining the relationship between crustal shortening and surface uplift of orogenic pla-

teaus remains a frontier problem in continental geodynamics. The second-largest modern orogenic plateau in the central Andes has been of particular interest because there is evidence for protracted deformation and crustal shortening since at least 40 Ma (Elger et al., 2005; Horton, 2005; McQuarrie et al., 2005; Oncken et al., 2006), but also recent surface uplift as young as 10 Ma that would postdate significant shortening (e.g., Gregory-Wodzicki, 2000; Garzzone et al., 2008; Hoke and Garzzone, 2008). From southern Peru to northern Argentina (~14°S–22°S), the Andes feature a high shortening retroarc fold-thrust belt (123–330 km, 37%–40%; Gotberg et al., 2010; McQuarrie, 2002) with peak elevations to ~5–6 km that form the eastern boundary of the ~3–4-km-high Altiplano plateau (Fig. 1A). In addition, the region is characterized by a prominent bend in both the continental margin and cordillera from Peru to Bolivia that is referred to as the Bolivian orocline (Carey, 1955) (Fig. 1). Work in the Altiplano–Bolivian orocline area has developed two differing bodies of data that argue for (1) protracted isostatic surface uplift due to tectonic shortening and crustal thickening (e.g., Isacks, 1988) or (2) rapid surface uplift in response to removal of the lower lithosphere (e.g., Garzzone et al., 2008). In either case, orogenic shortening should be able to account for both the modern crustal thickness as well as additional material that may have been removed. Available shortening estimates vary from fully accounting for modern crustal thickness (Müller et al., 2002; McQuarrie, 2002; Elger et al., 2005; McQuarrie et al., 2005) to predicting crustal deficits (Kley and Monaldi, 1998; Gotberg et al., 2010). However, the application of these two-dimensional (2-D) plane-strain shortening estimates to crustal thickness calculations is complicated by the kinematic system of the Bolivian orocline. Lithospheric thickening and delamination events, similar to scenarios proposed for the Altiplano, have been related to the 3-D kinematic system associated with orocline formation (Gutiérrez-Alonso et al., 2004, 2011).

Unraveling the complex 3-D kinematics of the Bolivian orocline requires accounting

for material displacements parallel to the orogenic trend (Kley, 1999; Hindle et al., 2005; Arriagada et al., 2008) and vertical axis rotations (Arriagada et al., 2006; Roperch et al., 2006) that are not resolved in 2-D cross sections. Internal strain is normally a critical part of the 3-D kinematic system in curved orogens (Yonkee and Weil, 2010), but has been shown to be negligible in the Bolivian orocline (Eichelberger and McQuarrie, 2015). Considering these factors in addition to age constraints is critical to accurately determining the influence of orocline deformation on the evolution of the crust and mantle lithosphere at the Altiplano. To achieve this, we present new high-resolution reconstructions of the Bolivian orocline with the goal of developing a more accurate kinematic model for the central Andes and Andean Plateau.

The reconstructions presented here focus on defining the 3-D kinematics of the Bolivian orocline and investigating how out-of-plane displacements have influenced crustal shortening at the central Andes and oroclines in general. Vertical axis rotation and strike-slip faulting have been shown to be the main mechanisms accommodating out-of-plane motion during the development of orogenic curvature (e.g., Kley, 1999; Arriagada et al., 2008). While the location and sense of offset on faults accommodating strike-slip displacements are now fairly well defined (Dewey and Lamb, 1992; Funning et al., 2005; Eichelberger et al., 2013), there are no direct controls on offset magnitude (Eichelberger et al., 2013). Permissible fault-parallel displacements can be estimated from reconstructions, but the reliability of these estimates is largely dependent on how well constrained the surrounding kinematics are. These reconstructions incorporate variable shortening magnitudes and directions; a range of possible limb rotations from global positioning system (GPS) and paleomagnetic data; and timing constraints from geology and thermochronology into a tightly constrained kinematic framework. Based on the results of these models, we can determine the collective effect of rotation and fault parallel motion on shortening at the Bolivian orocline.

\*Present address: StructureSolver LLC, Danville, California 94526, USA.

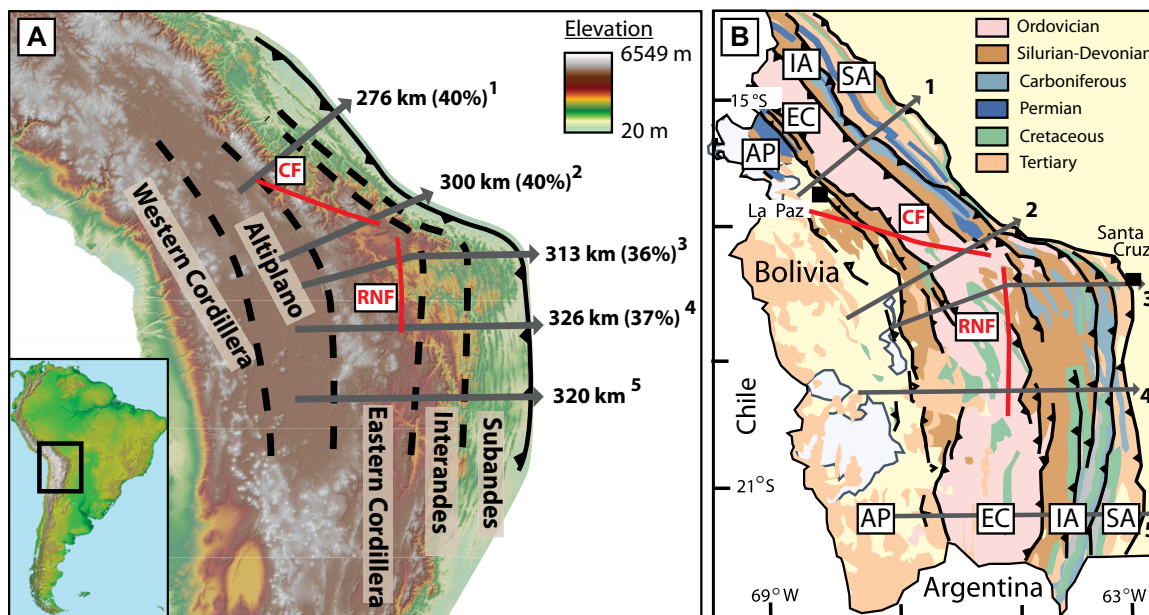


Figure 1. (A) Digital elevation model of the Bolivian orocline region (GTOPO30 1 km; U.S. Geological Survey global digital elevation model, 30 arc seconds, 1 km resolution; data available from the U.S. Geological Survey, <https://lta.cr.usgs.gov/GTOPO30>). Dashed lines show the approximate boundaries of the physiographic units. The Western Cordillera is the modern volcanic arc and the Altiplano is the 3–4-km-high, low-relief plateau. The retro-arc fold-thrust belt is composed of the high-elevation Eastern Cordillera (EC); the intermediate Interandean zone (IA); and the low-elevation modern deformation front at the Subandes (SA). Shortening estimates for the fold-thrust belt (AP, EC, IA, SA) are indicated by gray arrows, which point in the principal shortening direction for each section. Shortening magnitudes are reported for each line of section. RNF—Rio Novillero fault; CF—Cochabamba fault. Referenced sections: 1—McQuarrie et al. (2008); 2—McQuarrie (2002); 3—Eichelberger et al. (2013); 4—McQuarrie (2002); 5—Dunn et al. (1995), Kley (1996), Müller et al. (2002), Elger et al. (2005). (B) Simplified geologic map of the central Andean fold-thrust belt in Bolivia. Numbered cross-section lines as in A. Tertiary synorogenic sediments are dominantly exposed across the Altiplano basin and SA. In map view, the IA is characterized by Silurian–Cretaceous strata while the EC features Ordovician strata with Cretaceous–Tertiary preserved in synclinal basins.

## OROCLINE KINEMATICS

Out-of-plane motion has been shown to be a substantial factor in the development of orogenic curvature (e.g., Hindle and Burkhard, 1999; Yankee and Weil, 2010). In the central Andes, regional structural trends and paleomagnetic data imply that the Bolivian orocline is no exception. A northwest-southeast-trending structural fabric extending from southern Peru to central Bolivia defines the northern limb of the orocline (Fig. 1B). At the orocline axis in central Bolivia, this transitions to a north-south structural fabric that defines the southern orocline limb southward into Argentina and Chile. Based on geologic map patterns, the principle shortening directions of the limbs predict extension at the orocline core, but none is observed (Figs. 1B and 2A) (Kley, 1999; Eichelberger et al., 2013). Instead, paleomagnetic data and mapped strike-slip displacements indicate that the divergence of shortening directions in the

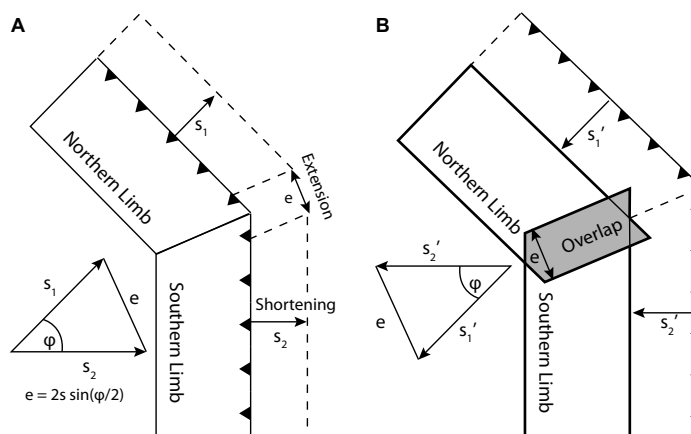


Figure 2. Schematic diagrams showing kinematics implied by plane-strain shortening estimates from the orocline limbs. (A) Modern case where divergent shortening directions in the orocline limbs imply extension as a function of the divergence in limb displacement directions ( $\phi$ ) and magnitude of limb shortening ( $s$ ) (modified from Kley, 1996). (B) Diagram of kinematic incompatibility that results from restoring orocline limb displacement based on plane-strain shortening estimates. In this case the magnitude of overlap, or kinematic incompatibility, is approximately equivalent to the magnitude of extension predicted in A.

## Bolivian orocline reconstruction

limbs is accommodated by out-of-plane displacement (Kley, 1999). Paleomagnetic data from across the central Andes characterize a regional pattern of counterclockwise rotations in the northern limb from Peru to northern Bolivia and clockwise rotations in the southern limb from southern Bolivia into northern Chile and Argentina (Fig. 3) (Arriagada et al., 2006; Barke et al., 2007; Roperch et al., 2006, 2011). Geodetic data indicate that orogenic curvature continues to evolve today with the potential for  $4^{\circ}$ – $10^{\circ}$  of limb rotation over the past 10 m.y. (Allmendinger et al., 2005). In addition to vertical axis rotations, earthquake focal mechanisms and geologic mapping indicate fault-parallel displacements on the Cochabamba fault (Dewey and Lamb, 1992) and Rio Novillero fault (Dewey and Lamb, 1992; Eichelberger et al., 2013) at the orocline core (Fig. 1). In prior reconstructions of the Bolivian orocline, fault-parallel displacements are crucial in restoring shortening in the absence of significant extension (Kley, 1999; Eichelberger et al., 2013).

The Carey (1955) classification of the central Andean curvature as an orocline carried the kinematic implication that the orogen was initially straight and underwent subsequent limb rotation and regional bending. Later work suggested that curvature developed due to a shortening gradient, increasing from the orocline limbs

toward the axis in central Bolivia (Isacks, 1988). However, the differences in Bolivian retroarc shortening are insufficient to fully account for paleomagnetic and GPS rotations, which suggests that curved slips paths or regional bending form a significant component of rotation (Eichelberger et al., 2013). As such, the modern orogenic curvature cannot be attributed to a shortening gradient alone, but the temporal overlap in vertical axis rotation and shortening indicate curvature developed contemporaneously with fold-thrust belt deformation.

## OROCLINE RECONSTRUCTIONS

Given the complexity of orocline kinematics, map-view reconstructions have long been recognized as the best tool for resolving shortening normal to structural trends as well as orogen-parallel motion (e.g., Laubscher, 1965). Where data and geologic constraints are sparse or nonexistent, the requirement of kinematic compatibility can provide predictions on displacement directions and magnitudes necessary for a self-consistent reconstruction (McQuarrie and Wernicke, 2005). Early reconstructions leveraged kinematic compatibility to predicted  $\sim 350$  km of shortening at the orocline axis for limb rotations of  $5^{\circ}$ – $10^{\circ}$  (Kley, 1999). However, the kinematic resolution of the model was

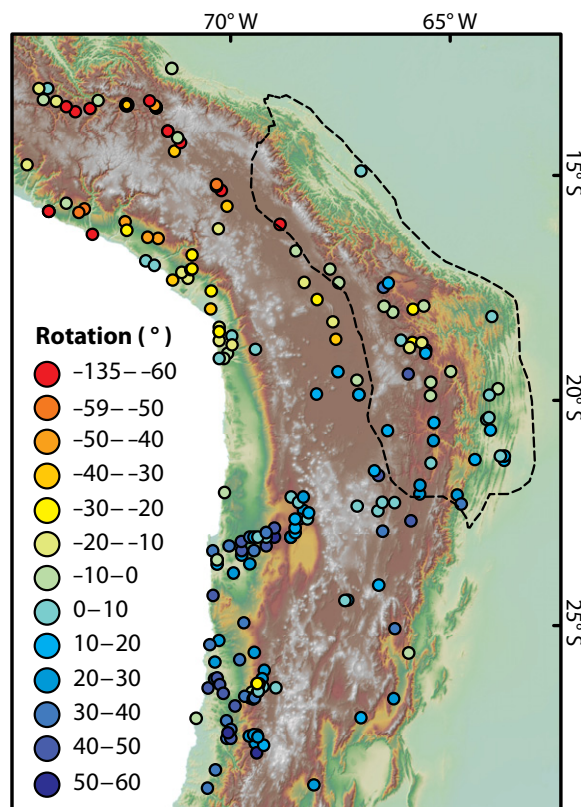
limited by sparse geologic mapping and paleomagnetic data as well as shortening estimates that underpredicted crustal thickness (Kley and Monaldi, 1998). Models constrained by paleomagnetic data (rather than shortening estimates) predicted  $\sim 400$  km of shortening at the orocline axis to restore forearc rotations that average  $\sim 30^{\circ}$  (Arriagada et al., 2008). These models focused on regional orocline bending rather than the specific kinematics of orocline deformation. Using updated structural geometry for the orocline core, simplified reconstructions predicted  $\sim 100$  km of orogen-parallel strike-slip displacements with  $\sim 14^{\circ}$  limb rotations (Eichelberger et al., 2013) but were limited in spatial extent.

None of the prior reconstructions fully incorporate both shortening estimates and paleomagnetic data at the structural resolution available in geologic maps. Mapping from the region (Kley, 1996; McQuarrie, 2002; Müller et al., 2002; Elger et al., 2005; McQuarrie et al., 2008; Eichelberger et al., 2013) has provided detailed control on variations in displacement direction and shortening magnitude that were unavailable or greatly simplified in previously published reconstructions. In general, these reconstructions also restore deformation in a single time step, but sufficient thermochronologic and geologic data sets now exist (Sempere et al., 1990; DeCelles and Horton, 2003; Horton and DeCelles, 1997; Horton, 2005; Uba et al., 2005, 2006, 2009; Gillis et al., 2006; Barnes et al., 2006, 2008, 2012; McQuarrie et al., 2008; Eichelberger et al., 2013) that constrain variations in deformation timing across the fold-thrust belt. The temporal component of deformation has been a missing aspect of prior reconstructions but is a critical variable in relating crustal thickening driven by orocline deformation to the timing of surface uplift.

## METHODS

To reconstruct orocline kinematics in a geographic context, this study utilizes an ArcGIS (geographic information system) based map-view reconstruction (Fig. 4A). The model covers the fold-thrust belt region of the Bolivian orocline and sequentially restores deformation from ca. 50 Ma to present in 5 m.y. increments. The restoration is driven using a Microsoft VBA (Visual Basic for Applications) script that calculates the positions of polygon centroids, displacing them at each time step based on vectors defined in an associated dBASE stable (after McQuarrie and Wernicke, 2005). The model accounts for vertical axis rotations by prescribing rotations about a polygon centroid, but for regional rotations each polygon's restoration path must be manually adjusted to reflect the regional change in displacement direction.

**Figure 3.** Overview of central Andean rotation pattern with the current paleomagnetic database for the central Andes (data from Arriagada et al., 2006; Roperch et al., 2006). Shaded topography is from Figure 1. Negative values indicate counterclockwise rotations and positive values are clockwise. Dashed black line indicates the boundary of the reconstructions presented in this study.



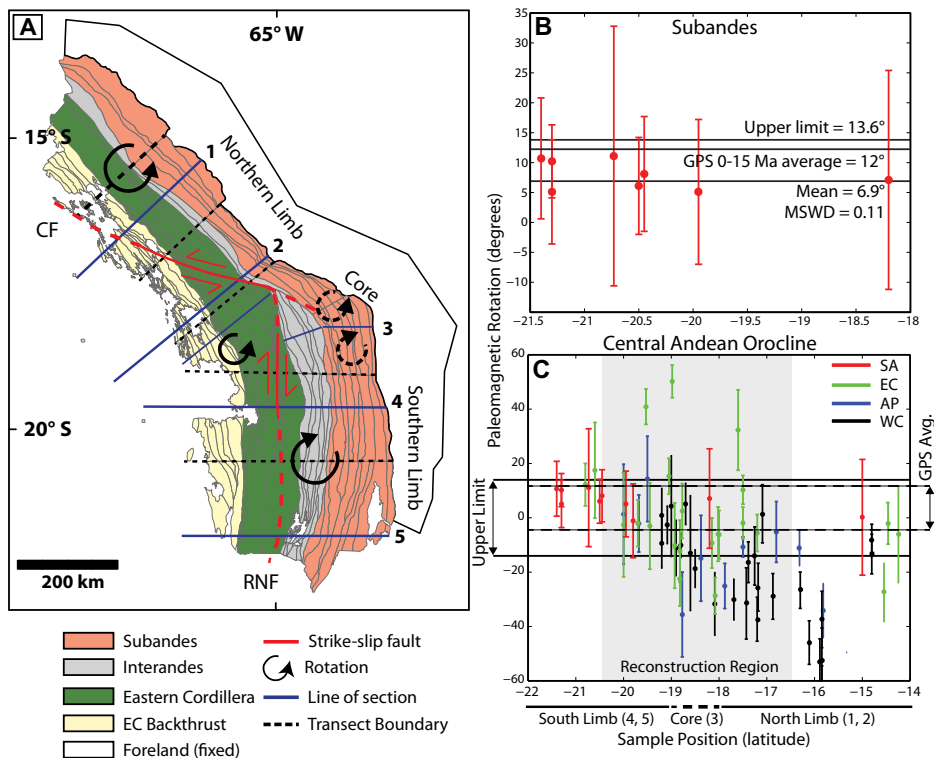


**Figure 4. Reconstruction setup.** (A) Model geometry with fault blocks outlined in gray and shaded based on physiographic unit. Blue lines show the location of balanced cross-section transects; numbers are as in Figure 1 and Table 1. Dashed black lines show the artificial transect boundaries used to allow for changes in shortening estimates and deformation timing. The locations of the Cochabamba (CF) and Rio Novillero (RNF) strike-slip faults are shown in red; arrows indicate the sense of offset. Rotational symbols show regional changes in rotation direction; solid symbols indicate prescribed rotation directions in the minimum and maximum rotation models while the dashed symbols (core Subandes) are added in the preferred model. EC—Eastern Cordillera. (B) The rotations used in the model are defined by paleomagnetic data from the Subandes (data from Roperch et al., 2006). The minimum rotation model is based on the mean of this data while the maximum rotation model is defined by the largest possible rotation within uncertainty. Extrapolated global positioning system (GPS) rotations (Allmendinger et al., 2005) are comparable to the upper limit of paleomagnetic rotation. MSWD—mean square of weighted deviates. (C) Plot of regional paleomagnetic data spanning the entire cordillera. The upper rotation limit from B is plotted by a solid line with the extrapolated GPS rotations plotted as a dashed line (Avg.—average). The rotations for the maximum rotation model encompass most of the paleomagnetic data from the fold-thrust belt in the reconstruction region. IA—Interandes; EC—Eastern Cordillera; AP—Altiplano basin; WC—Western Cordillera.

The viability of the proposed restoration paths can be assessed based on the self-consistency of the kinematic model through time (McQuarrie and Wernicke, 2005). Polygons that restore to overlapping positions indicate regions that violate strain compatibility due to defined restoration paths that are kinematically incompatible (McQuarrie and Wernicke, 2005). In the Bolivian Andes, deformation is principally characterized at both outcrop (McQuarrie and Davis, 2002) and regional scales (e.g., Sheffels, 1990; Kley, 1996; Lamb and Hoke, 1997; McQuarrie, 2002) by structures accom-

modating horizontal shortening perpendicular to structural trend. Balanced cross sections account for this plane-strain shortening; thus restoring Andean shortening estimates in map view requires the displacement direction be parallel to the line of section orientation and perpendicular to structural trend. Consequently, the restoration vectors in our reconstructions are initially defined by the magnitude of shortening directed normal to structural trend (Fig. 2A). Given the similarity of shortening estimates in the Bolivian Andes, kinematic incompatibilities largely arise from regional

changes in structural orientation that produce nonparallel restoration paths (Fig. 2B). Here we interpret the locations of kinematic incompatibilities to indicate regions where plane-strain deformation constraints are insufficient and additional components of out-of-plane motion are required (overlap in Fig. 2B). The magnitude of out-of-plane motion is approximately equal to the magnitude of extension predicted by the divergence in limb displacement directions. For the Bolivian orocline, recognized mechanisms for out-of-plane motion are regional paleomagnetic rotations and mapped strike-slip displacements along faults (Fig. 4). The objective is to restore both in-plane and out-of-plane deformation while minimizing the total kinematic incompatibility as quantified by the total overlap area at each time step. We test a range of permissible regional rotation magnitudes based on uncertainties in the available paleomagnetic and GPS data. Based on those results, additional strike-slip displacements are imposed along structures with geologic evidence for fault-parallel motion. The imposed displacements are kept at the minimum magnitude necessary to resolve large kinematic incompatibilities given the lack of direct constraints on strike-slip fault offsets. One limitation of the model is that polygon dimensions are fixed so the fault blocks are assumed to be rigid, ignoring internal strain. While this is a major simplifying assumption, recent work in the central Andes has shown that internal strain is negligible for the model region (Eichelberger and McQuarrie, 2015).

The fault-block boundaries are defined based on fault traces and fold axes from published geologic maps that range in scale from 1:100,000 to 1:500,000 (Fig. 4A) (e.g., Kley, 1996; Sheffels, 1988; McQuarrie, 2002; Müller et al., 2002; McQuarrie et al., 2008; Eichelberger et al., 2013). The blocks are regionally grouped into established physiographic zones present at the Bolivian orocline. From west to east, they are the Western Cordillera, Altiplano basin, Eastern Cordillera (EC), Interandean zone (IA), and Subandes (SA) (Fig. 1) (Isacks, 1988; Kley, 1996). The Western Cordillera is the modern volcanic arc with peak elevations of ~6 km and forms the western boundary of the ~3.8-km-high, internally drained Altiplano basin (Isacks, 1988). Due to extensive volcanic cover in the Western Cordillera, shortening is unconstrained and not included in the reconstructions presented here. The eastern limit of the Altiplano basin is defined by the EC, which has peak elevations of 5–6 km and is composed primarily of Paleozoic and Mesozoic rocks deformed by west-vergent folds and faults at the Altiplano basin–EC boundary. Structural

*Bolivian orocline reconstruction*

vergence direction in the EC switches from west (back thrust) to east (fore thrust) toward the EC–IA border (Fig. 5). The IA is characterized by 2–3 km elevations and dominantly Ordovician–Devonian strata involved in thin-skinned deformation (Kley, 1996; McQuarrie, 2002; Müller et al., 2002) (Fig. 1B). The SA is marked by elevations of <2 km and an 8–14 km structural elevation decrease from the IA (McQuarrie, 2002; Eichelberger et al., 2013) (Fig. 5). Geophysical data indicate that the change in structural elevation from the SA to IA is accommodated by basement deformation below the IA (Kley, 1996; Schmitz and Kley, 1997; Wigger et al., 1994; Dunn et al., 1995; Zapata and Allmendinger, 2000). The SA is structurally characterized by broad, linear synclines that form valleys containing Tertiary synorogenic sediments (Figs. 1B and 5). The synclines are separated by ridge lines sup-

ported by faulted anticlines involving Devonian through Cretaceous strata (Baby et al., 1992; Dunn et al., 1995; McQuarrie, 2002). Elevations decrease through the SA into the Chaco foreland basin where topographic relief diminishes to a low foreland slope (Barnes and Heins, 2009). The boundaries of each zone (Fig. 1B) are based on changes in structural elevation, proposed involvement of basement thrusts at depth, and changes in fault vergence direction (see Kley, 1996; McQuarrie and DeCelles, 2002; McQuarrie, 2002). To allow for variable restoration vectors and deformation timing along the Cordillera, the model includes artificial boundaries perpendicular to structural trend that separate the model into five transects (Fig. 4A). The transect boundary positions are based on the map-view extent of regions with balanced cross-section shortening estimates, but have no structural significance.

**DATA**

The principal kinematic constraints for the Bolivian central Andes come from shortening estimates from balanced cross sections, shortening directions from mapped fault and fold orientations, deformation timing from thermochronology and basin studies, and vertical axis rotations documented in paleomagnetic and GPS data. In addition, geologic mapping and earthquake focal mechanisms indicate strike-slip displacements at the orocline axis along extensive fault zones (Dewey and Lamb, 1992; Funning et al., 2005), but direct constraints on the displacement magnitude are not available.

The magnitude of displacement for each block is assigned based on fault offsets as shown in the cross sections associated with that transect (Table 1; Fig. 4A). The southernmost transect, unlike those to the north, lacks a single con-

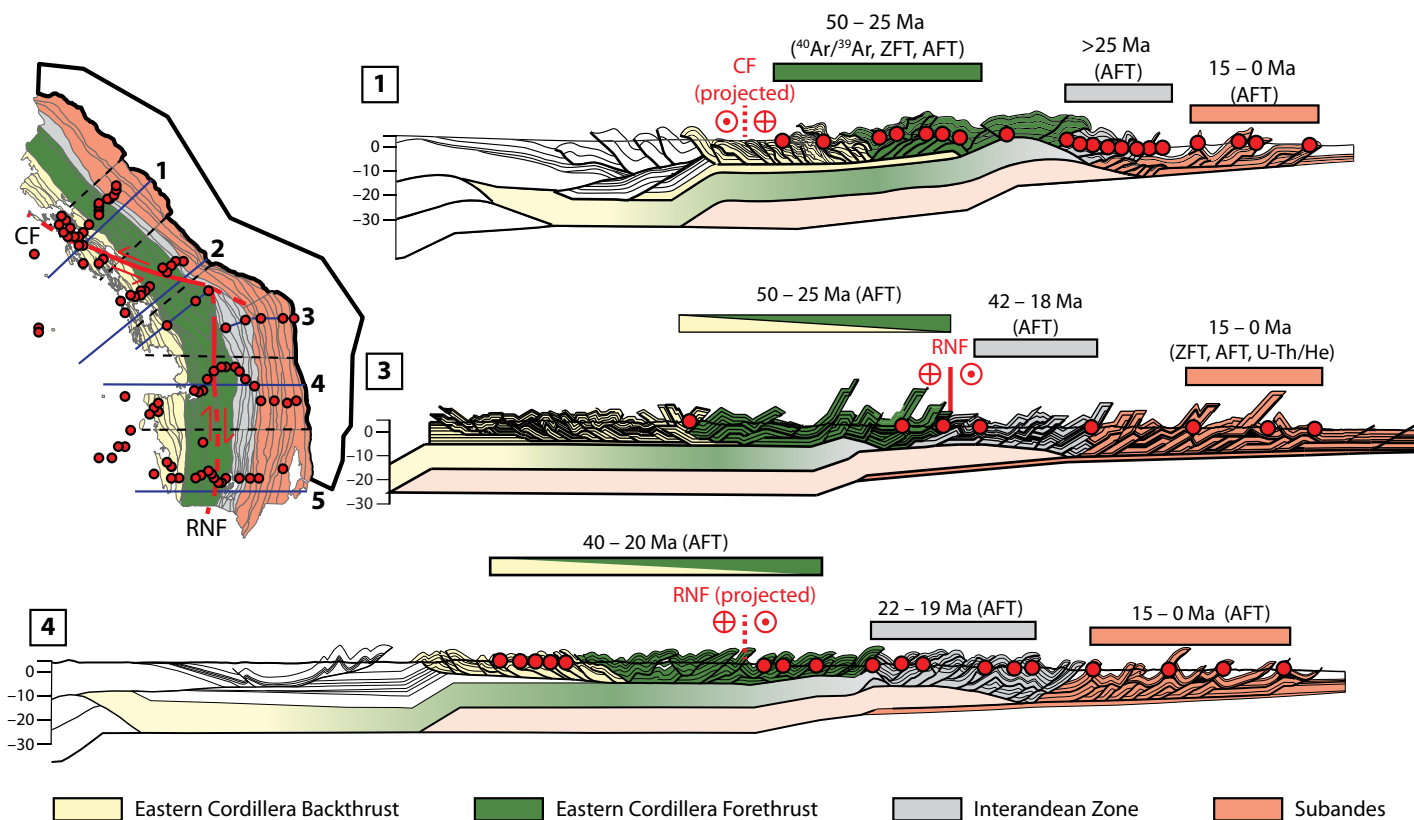


**Figure 5.** Representative balanced cross sections and thermochronology sample locations from the northern, central, and southern regions of the orocline. Map-view locations are approximate, cross-section locations are more specific. The cross sections are at equivalent scales and color coded based on their structural affinity. RNF—Rio Novillero fault; CF—Cochabamba fault. The lower basement thrust balances shortening in the Subandes while the upper basement thrust balances shortening in the Interandean zone, Eastern Cordillera, and Altiplano. The positions of thermochronology samples are shown by red dots. The time span of early cooling signals interpreted to reflect the onset of deformation is listed above each physiographic zone. Thermochronologic systems that define each cooling period are listed for each zone (AFT—apatite fission track; ZFT—zircon fission track). The width of the color-coded bars corresponds to the cross-sectional span of the data that defines each cooling period. References for each section: 1—McQuarrie et al. (2008); 3—Eichelberger et al. (2013); 4—McQuarrie (2002), Barnes et al. (2008).

TABLE 1. KINEMATIC CONSTRAINTS

	Shortening (km)	Rapid cooling (Ma)	Reference	Time step	Rotation (°)		
					Min	Max	Preferred
Transect 1a, 1b							
EC	123	45–25; 15–0	Barnes et al. (2006)	50–25	6	13	13
IA	48	before 25; 18–5	Gillis et al. (2006)	45–25	6	13	13
SA	66	15–0	McQuarrie et al. (2008)	15–0	6	13	13
Transect 2							
EC	142	55–21		50–25	6	13	13
IA	39	18–6	Barnes et al. (2012)	20–10	6	13	13
SA	71	10–5		10–0	6	13	13
Transect 3							
EC	136	50–25		50–25	6	13	13
IA	43	42–18	Eichelberger et al. (2013)	45–15	0	0	4
SA	86	15–0		15–0	0	0	±13
Transect 4							
EC	122	40–20		40–20	–6	–13	–13
IA	96	22–19	Barnes et al. (2008)	25–15	–6	–13	–13
SA	67	15–0		15–0	–6	–13	–13
Transect 5							
EC	95	40–20		40–20	–6	–13	–13
IA	62	18–9	Ege et al. (2007)	20–10	–6	–13	–13
SA	78	10–0	Scheuber et al. (2006); Uba et al. (2009)	15–0	–6	–13	–13

Note: EC—Eastern Cordillera; IA—Interandes; SA—Subandes; Min—minimum; Max—maximum.

tinuous line of section across the fold-thrust belt (transect 5, Fig. 4), so the total displacement is based on a composite shortening estimate from structural studies in each of the physiographic units (SA—Dunn et al., 1995; IA—Kley, 1996; EC—Müller et al., 2002). For fault blocks in all six transects, the shortening is restored in sequence, from east (SA) to west (EC). During restoration, active physiographic units are internally restored, indicated by expanding space between fault blocks. Outboard units to the west that have earlier deformation periods (restored in subsequent time steps) are passively displaced with no intraunit separation between fault blocks. Once a unit has been fully restored, the constituent fault blocks remain fixed. The primary challenge in reconstructing the orocline is that the curvature of the fold-thrust belt implies divergent plane-strain displacement paths that intersect as shortening is restored. Shortening magnitude estimates used for the reconstruction are quite similar and range from 276 km (40%) in the distal northern limb (McQuarrie et al., 2008) to 327 km (37%) in the southern limb (Table 1) (McQuarrie, 2002). The northwest-southeast structural fabric of the northern orocline limb implies a northeast principal shortening direction while the southern limb is characterized by a north-south structural fabric and east-directed shortening (Table 1; Fig. 4A).

### Timing

Timing of deformation in the model is based on a combination of thermochronologic cooling ages from each of the model transects and

geologic constraints from mapping and basin sedimentation histories. The available thermochronology data varies by transect, it generally includes  $^{40}\text{Ar}/^{39}\text{Ar}$ , zircon fission track, zircon (U-Th)/He, apatite fission track, and apatite (U-Th)/He ages from various stratigraphic depths and structural positions across all three major physiographic units (Fig. 5). These cooling ages have been used as a timing proxy for central Andes deformation under the assumption that cooling is driven by erosional exhumation in response to the relief generated by faulting (e.g., Barnes and Ehlers, 2009). Exhumation ages in each physiographic unit often overlap within uncertainty, preventing a fault-by-fault restoration sequence. The broad overlap in exhumation ages has been interpreted to reflect periods of distributed deformation both within each physiographic unit and across unit boundaries (Barnes et al., 2006, 2008; McQuarrie et al., 2008; Eichelberger et al., 2013). Rather than assuming a structure-by-structure propagation sequence, fault blocks within each physiographic unit are simultaneously restored over the same time period, beginning with the earliest exhumation age in that region (Fig. 5; Table 1). Overall, the oldest exhumation onset ages are found in the EC and generally become younger eastward into the SA (Barnes et al., 2006, 2008, 2012; McQuarrie et al., 2008; Eichelberger et al., 2013). While thermochronology can be used to interpret the onset of deformation within a physiographic region, determining the ages of cessation is more difficult. Geologic constraints show that deformation in the northern limb EC had ceased by 25 Ma (Gillis et al., 2006;

Horton, 2005) while GPS data and geomorphology indicate that the SA is actively deforming today (Brooks et al., 2011). There are no data that directly constrain the termination of IA deformation. However, the kinematic systems proposed in balanced cross sections suggest that IA deformation would have ceased by the time SA deformation was underway, although IA exhumation would continue (McQuarrie et al., 2008) (Fig. 5). In general, deformation in the SA is restored from 15 to 0 Ma across the entire orocline. Timing of IA exhumation varies by location, spanning 30–5 Ma in the northern limb, 40–15 Ma at the orocline axis, and 25–10 Ma in the southern limb. As a result, IA deformation is restored in the model beginning with the earliest exhumation age and ending at 15 Ma, when SA deformation begins. In the EC, fault blocks are restored over 45–25 Ma in the northern limb, 50–20 Ma at the orocline axis, and 50–20 Ma for the southern limb.

### Rotation

At the regional scale, paleomagnetic and GPS data from Peru to Chile resolve the central Andean rotation pattern system of counterclockwise rotations in the northern limb and clockwise rotations for the southern limb (Figs. 3 and 4). At smaller scales, the rotations are subject to local structural influences, have large uncertainties, and were sampled from lithologies older than Late Cretaceous that may record rotations unrelated to Andean deformation. In addition, the data are concentrated in volcanic forearc rocks but sparse in the portion of the retroarc fold-thrust belt covered by the reconstruction. Collectively, these factors make it difficult to identify rotations related to the development of orogenic curvature. To determine representative magnitudes of rotation related to recent Andean deformation, we focus on paleomagnetic data from synorogenic sediments located in the SA (compiled by Roperch et al., 2006). The SA definitively accommodated the most recent phase of deformation in the central Andes from ca. 15 Ma to present. SA structures are dominantly fault-propagation folds with consistently linear local orientations, typical of foothills-style deformation (Dahlstrom, 1969). There is little evidence for structural complexities that could result in local block rotations, suggesting that rotations recorded by Tertiary synorogenic sediments document regional rotation. In addition, GPS data (Allmendinger et al., 2005) provide additional constraints on regional rotations. Extrapolating modern rotations over geologic time assumes constant rotation rates; however, at a regional scale, the convergence direction for the subducting Nazca plate has been constant

since SA deformation began ca. 15 Ma (Pardo-Casas and Molnar, 1987; Somoza, 1998). Modeling the rotational component of oroclinal bending as contemporaneous with shortening in the SA differs from interpretations that attribute bending of the Andes to regional north-south compression unrelated to fold-thrust belt shortening (e.g., Johnston et al., 2013). Given that the SA in the model area has been actively exhuming since at least 5 Ma (Barnes et al., 2006, 2008, 2012; Eichelberger et al., 2013), continues to shorten today (Brooks et al., 2011), and modern backarc rotation rates are low ( $\leq 2^\circ$  m.y.<sup>-1</sup>; Allmendinger et al., 2005), it is unlikely that rotational bending postdates SA deformation.

Due to the large uncertainties in the paleomagnetic data, we perform two reconstructions to test minimum and maximum magnitudes of limb rotation. Paleomagnetic rotations in the southern limb SA between 21.5°S and 18°S range from  $-1.1^\circ \pm 14^\circ$  (counterclockwise) to  $11.1^\circ \pm 22^\circ$  (clockwise) (Fig. 3). Two SA data points are available for the northern limb, recording  $0.2^\circ \pm 21^\circ$  at 15°S and  $-7.4^\circ \pm 7.2^\circ$  at 12.7°S. These measurements are statistically equivalent, but within the context of the central Andean rotation pattern, we assume that  $-7.4^\circ \pm 7.2^\circ$  is consistent with orocline scale deformation and complimentary to south limb rotation. The minimum rotation scenario is based on the mean SA rotation ( $\sim 7^\circ$ ; Table 1; Fig. 4B). The maximum rotation scenario is based on the maximum permissible rotation within uncertainty for the SA paleomagnetic data in the study region. In the reconstruction, the maximum rotation applied to the limbs is  $13^\circ$  (Table 1; Fig. 4B). The rotational range represented by the minimum and maximum rotation scenarios cover retroarc GPS rotations extrapolated over 15–0 Ma (south limb:  $12^\circ$ ; north limb:  $-6^\circ$ ; Allmendinger et al., 2005) as well as the range of EC and Altiplano basin paleomagnetic rotations from the reconstruction region (Fig. 4C). Paleomagnetic rotations in the EC region of the orocline core are variable, likely due to the influence of possible strike-slip faulting in the area of Cochabamba where the available samples are located. Minimal rotations have been predicted for this region (Kley, 1999; Arriagada et al., 2008); however, the northwest-southeast-trending EC structures at the core are continuous with northern limb structures that undergo counterclockwise rotations. For the initial maximum and minimum limb rotation models, the core EC rotates with the northern limb while the IA and SA do not rotate (Fig. 4B).

The most prominent effect of restoring regional rotations is the progressive impact it has on changing the displacement directions defined in each region. The reconstruction assumes that

rotation was a function of SA deformation: blocks that underwent less displacement also underwent a proportionally lower magnitude of rotation. Within the model framework, the magnitude of rotation restored at each time step during SA deformation is scaled by a given fault block's displacement magnitude. Therefore, as with shortening, rotations are restored in sequence from the SA (recent deformation) back toward the EC (earlier deformation). Additional rotations can be added at earlier time steps to resolve local kinematic incompatibilities, but are not required because SA rotations account for measured EC rotations within uncertainty (Fig. 4C). By the time the SA is fully restored, blocks at the western edge of the SA and beyond undergo the full magnitude of assigned limb rotation. The incremental rotations at each time step then alter fault-block displacement paths in all subsequent time steps. The regional displacement direction in the minimum rotation model changes from  $270^\circ$  (west) to  $262^\circ$  (approximately west-southwest) in the southern limb and from  $229^\circ$  (approximately south-southwest) to  $237^\circ$  (approximately southwest) in the northern limb. The maximum rotation model displacement directions change to  $256^\circ$  (approximately west-southwest) in the southern limb and from  $243^\circ$  (approximately southwest) in the northern limb. Independently restoring the limb rotations and shortening translations in each transect imposes different poles of rotation for north and south limbs (similar to the external pivot model of Sussman et al., 2012). The poles are located away from the orocline axis and outside the reconstruction reference frame. Consequently, the only fixed points in the area of the reconstruction are along the modern foreland basin.

### Strike-Slip Displacements

Of all the kinematic components documented at the Bolivian orocline, the magnitude of lateral displacements approximately parallel to fault trend is the least well constrained. Geologic and seismologic evidence shows that at least two faults have accommodated transpressional deformation in the region of the orocline axis and continue to do so today. The north-south-trending Rio Novillero fault (RNF, Fig. 6) at the orocline core was initially located based on the change from northeast-vergent thrust faults that characterize the north limb structural fabric to east-vergent structures characteristic of the south limb (Dewey and Lamb, 1992). This change occurs abruptly across several structures that have accommodated north-south-oriented, right-lateral motion indicated by locally offset lithologic contacts, but no direct constraints on

the total north-south displacement are available (Eichelberger et al., 2013). Recent seismicity in the area also shows that the RNF accommodates right-lateral motion on nearly vertical faults planes today (Fig. 6) (Dewey and Lamb, 1992; Funning et al., 2005). The Cochabamba fault has been mapped as both a normal and left-lateral fault (Dewey and Lamb, 1992; Kennan et al., 1995; McQuarrie, 2002; Sheffels, 1995) due to the presence of two apparent pull-apart basins with bounding ranges that are 2–3 km higher in elevation (Cochabamba fault, CF, Fig. 6). Earthquake focal mechanisms are consistent with left-lateral fault displacements (Dewey and Lamb, 1992), but there are no geologic observations that constrain offset magnitude. Together the RNF and CF are proposed to form a conjugate fault system (Dewey and Lamb, 1992) that structurally separates the orocline core from the limbs, similar to the orocline model of Kley (1999). The extent of both faults beyond the orocline core region is ambiguous, but for different reasons. The regional change in structural trend associated with the RNF is traceable for  $\sim 100$  km until the structural trend becomes uniformly north-south in the southern limb (Fig. 6). The southern limb extension of RNF in the model follows east-vergent thrust faults where bedding orientations are slightly oblique to fault trend, similar to the structural relationship established to the north (Fig. 4A). The extent of the CF is best defined by the west-east-trending pull-apart basins, oblique to the northwest-southeast structural fabric. These features are only discernable over  $\sim 50$  km, suggesting that if the CF extends westward into the northern limb and Altiplano, fault-lateral offsets are probably distributed along the northwest-southeast-trending thrust faults that characterize the region west of the Cochabamba basins. In the model, the CF is extended westward following mapped thrust faults that are slightly oblique to the dominant trend but become parallel to the regional trend closer to the Altiplano (Fig. 4A). Where the RNF and CF parallel the local fold-thrust belt trend, any lateral displacement would be convolved with fault-normal shortening, making the lateral component of slip difficult to detect in the field. Lateral displacements are not mapped in the limbs, which suggests that the total offset on either fault system may be small and distributed over multiple faults.

### RESULTS

In all of the reconstructions presented here, the kinematic incompatibility of a given time step is interpreted based on the total overlapping polygon area at that time step. The total overlap area at the final time step is the cumula-

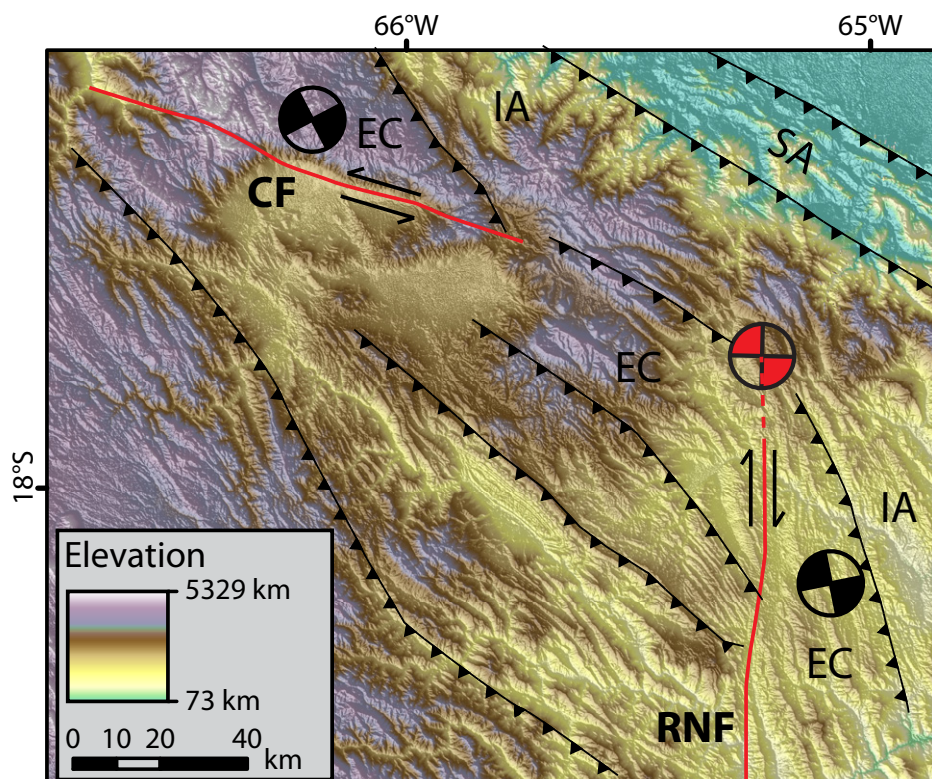


**Figure 6.** Digital elevation model of the orocline core region (ASTER 30m; Advanced Spaceborne Thermal Emission and Reflection Radiometer, 30 m resolution). The mapped locations of the Cochabamba (CF) and Rio Novillero (RNF) faults are shown in red. Major thrust faults are shown in black to show the changes in fault vergence direction across the RNF. Earthquake focal mechanisms from Dewey and Lamb (1992) are shown in black. The focal mechanism for the 1998 Aiquile  $M_w$  6.6 earthquake is shown in red. InSAR (interferometric synthetic aperture radar) preferred fault-plane solution is right-lateral offset (Funning et al., 2005). EC—Eastern Cordillera; IA—Interandes; SA—Subandes.

tive overlap from the entire model. However, for a physiographic region in a given transect, the maximum overlap magnitude may occur at an earlier time step. For example, the magnitudes of SA overlap in each model peaks when SA shortening has been fully restored then remains fixed in subsequent time steps. Since the IA and EC have concurrent restoration periods (ca. 45–20 Ma, depending on transect), peak overlap magnitudes may decrease as shortening is restored in adjacent zones and the area between polygons increases. In terms of improving the kinematic model by including fault-parallel displacements to minimize the overlap area, the location and time of overlap is as important as the magnitude. However, changes in a physiographic region's overlap magnitude between time steps can reveal if imposing out-of-plane motions actually improves kinematic compatibility or if it simply transfers incompatibilities to other regions. To summarize the results of each reconstruction, we report the total overlap from the final time step as the total kinematic

incompatibility and use it to compare reconstruction results. For regions with imposed fault-parallel displacements, local overlap magnitudes (overlap within a physiographic region of a transect) are compared at individual time steps to analyze whether out-of-plane movement resolves or redistributes kinematic incompatibility.

The magnitude of overlap area produced in a reconstruction using only plane-strain restoration constraints provides a benchmark for determining relative improvement in kinematic compatibility with increasing kinematic complexity (Fig. 7). Without rotation or fault-parallel displacements, the total kinematic incompatibility at the final stage of the restoration is 14,160 km<sup>2</sup>. Of the total overlap, the majority (11,400 km<sup>2</sup>, 80%) results from the intersection of the southwest-directed restoration path of the core with the west-directed south limb restoration path. No kinematic incompatibilities arose in the north limb. There are secondary regions of kinematic incompatibility in the orocline core

that peak prior to the final time step due to the sequence of restoration. SA overlap (1000 km<sup>2</sup>) peaks at 15 Ma and the EC overlap (2500 km<sup>2</sup>) peaks at 25 Ma (Fig. 8A). These kinematically incompatible areas at the orocline core are due to internal changes in structural trend that are not found in either of the limbs (Fig. 7).

The minimum limb rotation ( $\pm 7^\circ$ ) reconstruction (Fig. 9) results in substantially less kinematic incompatibility with the final magnitude of overlap dropping to 5300 km<sup>2</sup>, >60% less overlap area than the plane-strain model (Fig. 8B). The regional reduction in overlap magnitude is largely due to the inclusion of limb rotation, which alters the limb displacement paths so that they are closer to parallel. Kinematic compatibility was further improved by imposing  $\sim 90$  km of south-directed, fault-parallel slip along the RNF over 50–0 Ma to eliminate overlap between the core and south limb EC in transect 4 (Fig. 9; Table 2). However at the local scale, propagating slip on the RNF into the southern limb increases EC overlap in transects 5 and 6 (Figs. 4 and 9). As a result the greatest total overlap ( $\sim 7000$  km<sup>2</sup>) occurs at 25–20 Ma as the RNF propagates south, but this overlap subsequently decreases as the southern limb EC is restored (Fig. 8B). Overall, the reduction in overlap from the plane-strain model outweighs any local increases, but the introduction of localized kinematic incompatibilities in the south limb from RNF slip indicates that it may not be kinematically viable for the fault to accommodate  $\sim 90$  km of north-south slip. Instead, larger limb rotations and/or the inclusion of slip on the CF may be required to resolve the incompatibility of the core and southern limb displacement directions. The kinematic incompatibilities within the orocline core show no reduction in the IA and SA but are reduced in the EC (Fig. 8B). This is because the northwest-southeast-trending EC structures are allowed to rotate with the north limb from 15 to 0 Ma whereas the IA and SA do not rotate. IA and SA overlap at the core both peak at 15 Ma, then IA overlap decreases as deformation is restored from 20 Ma onward (Figs. 4B and 9).

Increasing the magnitude of limb rotation to the upper permissible limit of  $\sim 13^\circ$  further improves kinematic compatibility (Fig. 10) with a final overlap area of 3200 km<sup>2</sup>, an  $\sim 80\%$  decrease over the final overlap in the plane-strain model (Fig. 8C). With the larger limb rotations,  $\sim 45$  km of north-south slip on the RNF was required to resolve kinematic incompatibilities between the core and southern limb, roughly half the magnitude required by the minimum limb rotation model (Table 2). Lower RNF displacement also introduced less kinematic



*Bolivian orocline reconstruction*

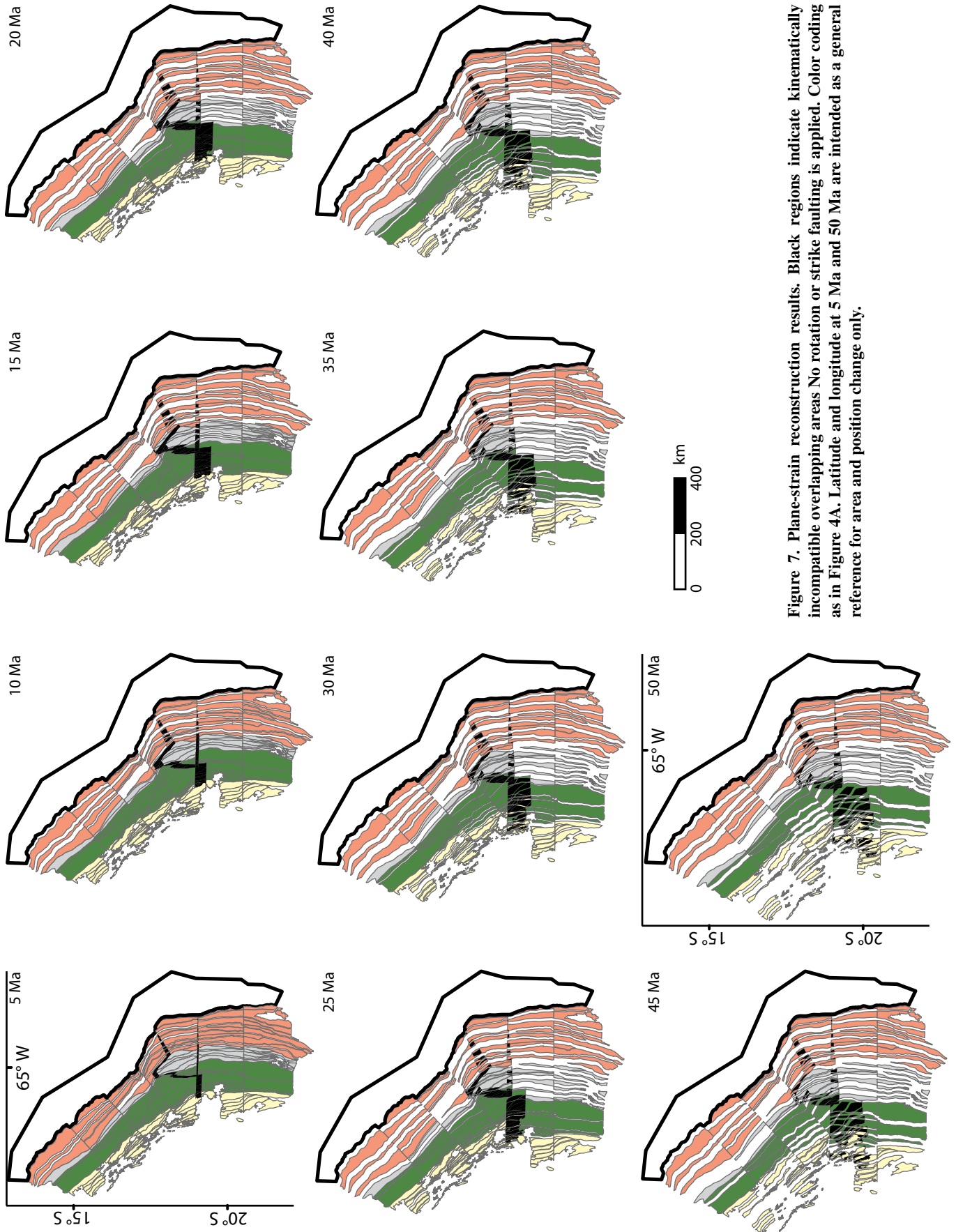


**Figure 7. Plane-strain reconstruction results. Black regions indicate kinematically incompatible overlapping areas. No rotation or strike faulting is applied. Color coding as in Figure 4A. Latitude and longitude at 5 Ma and 50 Ma are intended as a general reference for area and position change only.**

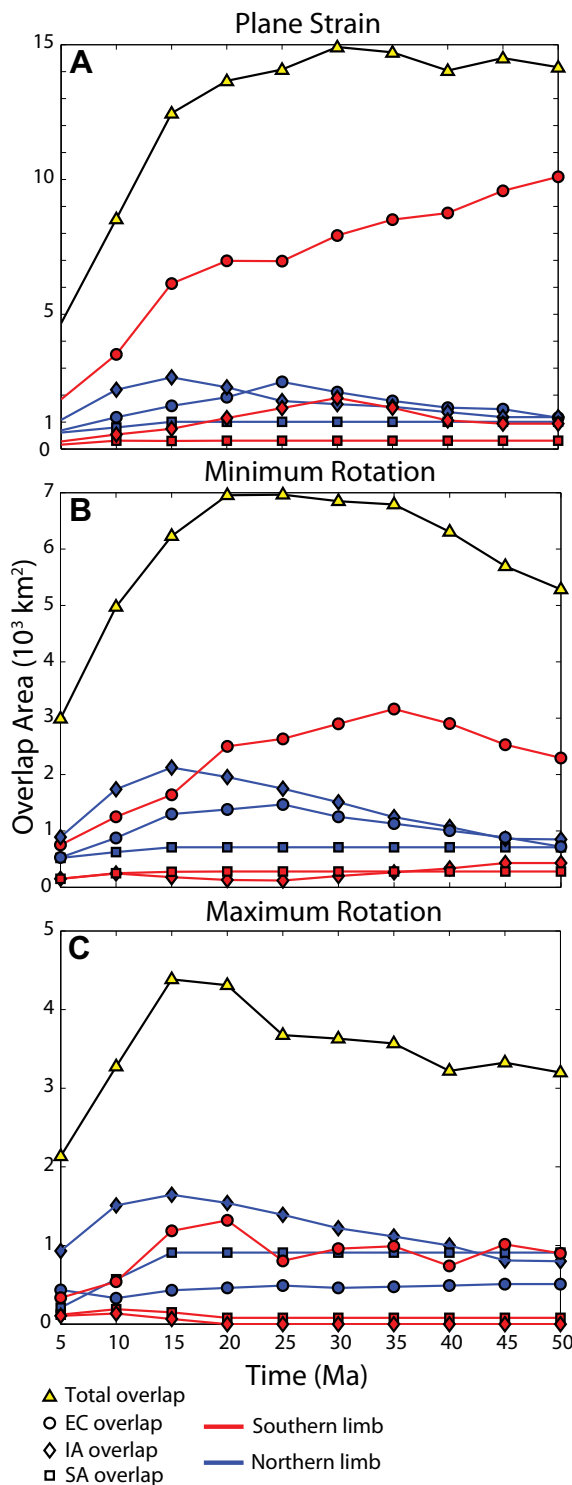


**Figure 8.** Plot of overlap area at each time step. (A) Plane-strain model. (B) Minimum rotation model. (C) Maximum rotation model. Shapes correspond to each physiographic region, colors indicate position in the orocline. The northern limb is not included because no overlap occurs there. EC—Eastern Cordillera; IA—Interandes; SA—Subandes.

incompatibility in the south limb, as shown by peak south limb EC overlap of 1300 km<sup>2</sup> at 20 Ma (Fig. 8C) compared to ~3000 km<sup>2</sup> at 35 Ma in the minimum rotation model (Fig. 8B). Overall, the larger limb rotations greatly improved the kinematic compatibility of the core and southern limb while reducing the

magnitude of slip required on the RNF, and by extension, the magnitude of overlap introduced in the southern limb. Within the orocline core, local kinematic incompatibilities related to changes in structural orientation remain unresolved in this model. The total overlap area for the maximum rotation model peaked at 15 Ma

(~4400 km<sup>2</sup>), at which time incompatibilities in the core IA and SA account for ~60% (2560 km<sup>2</sup>) of the total overlap area (Fig. 8C). The next largest overlap component at 15 Ma is related to north-south slip on the RNF in the south limb EC (~1200 km<sup>2</sup>) and composes 30% of the total 15 Ma overlap (Fig. 8C). Further improving the kinematic compatibility of the reconstruction will require a solution that can account for the changes in structural trend at the orocline core and further reduce the amount of RNF slip required to mitigate overlap between the southern limb and orocline core.

**DISCUSSION**

Overall, the maximum rotation model had the lowest magnitude of overlap at every time step (Fig. 8C) and imposed far lower strike-slip displacements on the RNF. Regional limb rotation resulted in displacement paths that were closer to parallel, resolving many of the regional incompatibilities related to intersecting plane-strain shortening directions (Fig. 11). In turn, this reduced the magnitude of fault-parallel displacement interpreted at the orocline core in order to resolve kinematic incompatibility between the core and southern limb. We believe that this indicates that at least ~13° of rotation in both limbs is required to achieve greatest degree of kinematic compatibility in a reconstruction with the current constraints available. This is slightly larger than the 5°–10° of rotation estimated by Kley (1999), but agrees with GPS rotation magnitudes extrapolated over the 15–0 Ma SA deformation window (Allmendinger et al., 2005). For the region of the fold-thrust belt covered by this reconstruction (14.6°S–22.5°S), 13° limb rotations used are within the range of solutions proposed by Arriagada et al. (2008).

**Preferred Model**

Even in the maximum rotation model, localized areas of overlap persist at the orocline axis despite the regional improvement in kinematic compatibility. In addition, introduced kinematic incompatibility related to slip on the RNF in the southern limb suggests that large right-lateral offsets may not be viable there. The CF was considered fixed for the minimum and maximum rotation models, but may have accommodated transpressional deformation based on its oblique orientation relative to the surrounding EC structural fabric (Fig. 6). Further refining the core kinematics to reduce the remaining overlaps beyond the available constraints can resolve local incompatibilities as well as elucidate the role of the CF in accommodating deformation at the core.

*Bolivian orocline reconstruction*

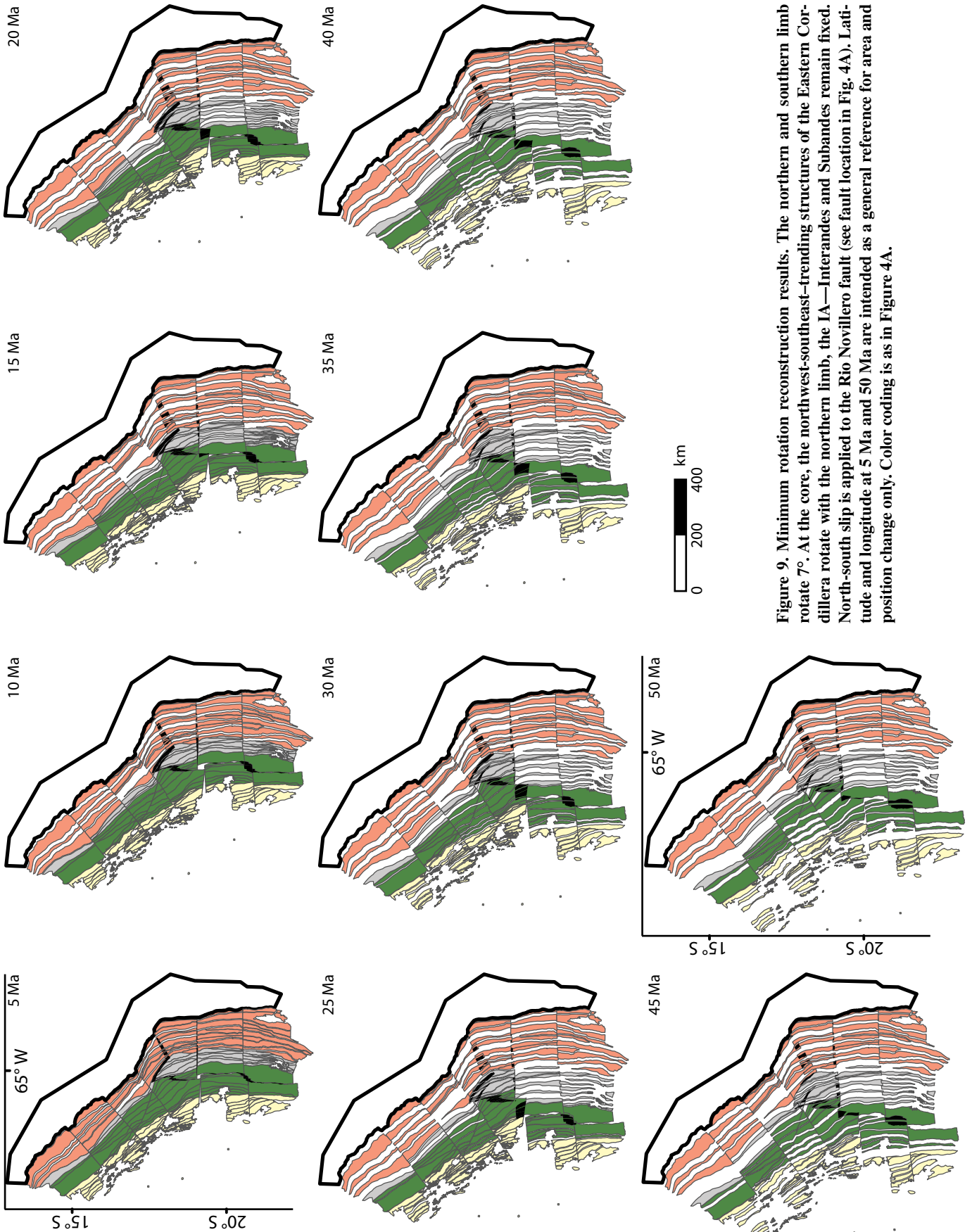


**Figure 9.** Minimum rotation reconstruction results. The northern and southern limb rotate 7°. At the core, the northwest-southeast-trending structures of the Eastern Cordillera rotate with the northern limb, the IA—Interandes and Subandes remain fixed. North-south slip is applied to the Rio Novillero fault (see fault location in Fig. 4A). Latitude and longitude at 5 Ma and 50 Ma are intended as a general reference for area and position change only. Color coding is as in Figure 4A.

TABLE 2. COMPARISON OF SHORTENING MAGNITUDES

Transect	Shortening (km)						AP	Total map-view shortening (km)	CF slip (km)	Timing (Ma)	RNF slip (km)	Timing (Ma)	Additional map-view shortening (km)			Total shortening difference (km)
	SA		IA		EC								RNF	CF	SA	
Minimum rotation model																
1a	66	77	48	48	123	125	40	290	0	N.A.	0	N.A.	0	0	11	13
1b	66	78	48	48	123	123	40	289	0	N.A.	0	N.A.	0	0	12	12
2	71	80	39	39	142	142	47	308	0	N.A.	0	N.A.	0	0	9	9
3	86	86	43	45	136	136	47	214	0	N.A.	0	N.A.	0	0	0	2
4	67	76	96	94	122	200	41	411	0	N.A.	90	50–0	78	0	9	85
5	78	87	62	70	95	166	41	364	0	N.A.	90	50–0	71	0	9	88
Maximum rotation model																
1a	66	90	48	50	123	125	40	305	0	N.A.	0	N.A.	0	0	24	28
1b	66	95	48	50	123	123	40	308	0	N.A.	0	N.A.	0	0	29	31
2	71	90	39	37	142	138	47	312	0	N.A.	0	N.A.	0	0	19	13
3	86	87	43	45	136	140	47	319	0	N.A.	0	N.A.	0	0	1	7
4	67	85	96	95	122	146	41	367	0	N.A.	50	50–0	24	0	18	41
5	78	100	62	60	95	120	41	321	0	N.A.	50	50–0	25	0	22	45
Preferred model																
1a	66	90	48	50	123	186	40	366	50	25–0	0	N.A.	0	63	24	89
1b	66	90	48	50	123	190	40	370	50	25–0	0	N.A.	0	67	24	93
2	71	90	39	97	142	210	47	384	50	25–0	0	N.A.	0	68	19	85
3	86	105	43	80	136	158	47	390	0	N.A.	<10	15–0	59	0	19	78
4	67	83	96	97	122	125	41	346	0	N.A.	<10	15–0	3	0	16	20
5	78	100	62	61	95	100	41	302	0	N.A.	<10	15–0	5	0	22	26

Note: SA—Subandes; IA—Interandes; EC—Eastern Cordillera; AP—Altiplano; CF—Cochabamba fault, left-lateral slip; RNF—Rio Novillero fault, right-lateral slip; CS—cross-section shortening; MV—map view shortening; N.A.—not applicable, no fault slip applied.

To investigate these possibilities, we present an additional, preferred model that builds on the results from the maximum rotation model (Fig. 12). For the orocline limbs, displacement magnitude, limb rotation, and timing are all kept the same. At the orocline core we prescribe SA rotation to be equivalent to limb rotation magnitudes and impose small rotations in the core IA and EC as well as fault-parallel offsets on the CF to resolve remaining internal core overlaps. As with the EC, northwest-southeast-trending SA fault blocks rotate with the northern limb while more north-south-trending SA blocks rotate with the southern limb (dashed rotation lines, Fig. 4A). The final overlap with these adjustments is ~1600 km<sup>2</sup> with a peak overlap of 1900 km<sup>2</sup> at 15 Ma for a ~50% reduction in peak and final overlap from the maximum rotation model (Fig. 13).

By allowing the core SA to rotate the full magnitude of limb rotation, the internal overlap decreases slightly from 900 km<sup>2</sup> to 700 km<sup>2</sup>. Slight differences in the structural orientation of the SA in the core and southern limb result in a shift of some SA overlap to the southern limb, increasing overlap from <100 km<sup>2</sup> in the maximum rotation model to ~600 km<sup>2</sup>. The total magnitude of SA overlap remains similar (1400 km<sup>2</sup> compared to 1000 km<sup>2</sup> in the maximum rotation model), indicating that the internal SA overlap was redistributed southward (Fig. 13). The remaining SA kinematic incompatibility at the core is related to the gradual change in SA structural orientation in the area, implying local, nonparallel displacement directions (Fig. 4A). A possible solution would be small but dis-

tributed fault-parallel displacements along the north-south-trending SA structures, similar to the model of Kley (1999).

As with the first two models, northwest-southeast-trending EC blocks defined by structures west of the RNF rotated with northern limb but at a lower magnitude (~5° instead of 13°; Fig. 4A). The EC and IA structures east of the RNF had no defined rotation in the first two models, but here are rotated ~5° with the southern limb based on their close alignment with the north-south southern limb fabric. In effect, the RNF becomes a rotational boundary that accommodates transpression related to the counter rotation of the two structural domains. By allowing the north-south EC and IA structures at the core to counter rotate, we resolve all the internal core overlap related to the east to west change in structural orientation between the SA, IA, and EC (cf. IA overlap in Figs. 8C and 13). Slip along the CF was applied to accommodate both the counter rotation of the northwest-southeast and north-south structural domains and shortening within the IA at the orocline core. By allowing ~50 km of left-lateral CF slip over 25–0 Ma (Table 2), kinematic incompatibility between the EC at the orocline core and the southern limb was largely eliminated. This is equivalent to the magnitude of right-lateral RNF slip from the maximum rotation model, but has the advantage of not producing additional overlap in the limbs. The majority of orogen-parallel strike-slip motion occurs on the CF in this model while the RNF accommodates <10 km of right-lateral motion.

### Transpressional Deformation

In the preferred model the RNF and CF behave as a conjugate fault system (Dewey and Lamb, 1992). However, rather than accommodating purely strike-slip motion, the reconstruction suggests that both accommodated out-of-plane transpressional deformation that was not previously recognized (Fig. 12). For the RNF, the preferred model estimates ~40–50 km of strike-normal shortening, which we have distributed across 4 fault blocks between the RNF and the IA-EC boundary over 25–15 Ma and concentrated along the RNF trace from 15 to 0 Ma (Table 2). The preferred model estimates ~60–70 km of strike-normal shortening on the CF from 45 to 0 Ma (Table 2). This amount of shortening is a function of how the IA is restored at the orocline core from 45 to 15 Ma, but is currently not accounted for in shortening estimates in the region. Less than 20 km of CF shortening occurred from 15 to 0 Ma, because the IA and EC were inactive. As a result, motion on the CF was dominated by the strike-slip displacements imposed to resolve kinematic incompatibility. The geologic map patterns for both faults (McQuarrie, 2002; Eichelberger et al., 2013) do not rule out the possibility of significant shortening, but most thrust faults in the central Andes have offsets <15 km (e.g., McQuarrie, 2002). This suggests that transpression is most likely distributed over several structures rather than localized to the degree modeled here. The CF region has higher structural elevations and deeper exposed

*Bolivian orocline reconstruction*

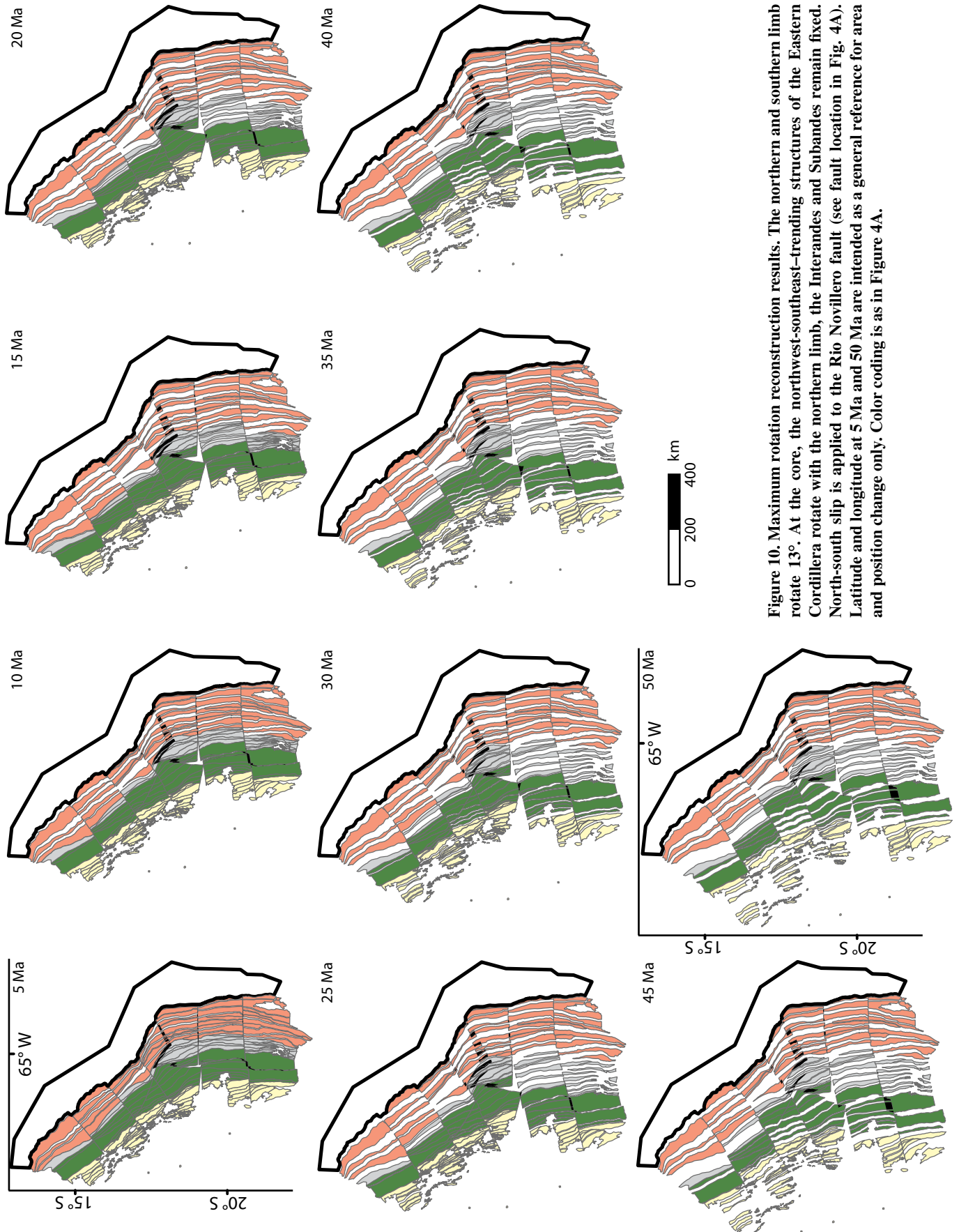


**Figure 10.** Maximum rotation reconstruction results. The northern and southern limb rotate 13°. At the core, the northwest-southeast-trending structures of the Eastern Cordillera rotate with the northern limb, the Interandes and Subandes remain fixed. North-south slip is applied to the Rio Novillero fault (see fault location in Fig. 4A). Latitude and longitude at 5 Ma and 50 Ma are intended as a general reference for area and position change only. Color coding is as in Figure 4A.

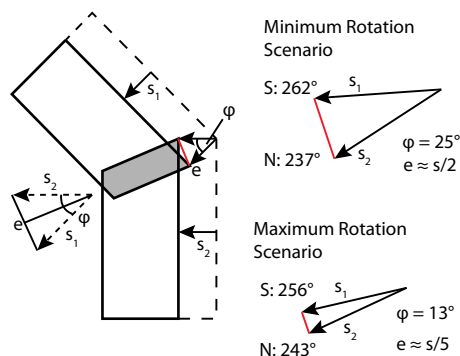


**Figure 11. Schematic diagram of the effect of accounting for rotation on plane-strain displacement paths (see text and Fig. 2). As displacement paths rotate closer to parallel (larger limb rotations), the magnitude of predicted overlap decreases (as shown in Fig. 2A).**

stratigraphy than the RNF region, consistent with localized shortening. The CF also features large transensional basins with 2–3 km of relief, indicating nontrivial offsets along the fault. Comparatively, the RNF has only minor topographic expression and is largely defined by the change in structural orientation across the apparent fault trace.

The CF and RNF are both located within the EC, which is restored over 50–25 Ma in this reconstruction (Fig. 12). As such, the transpression displacements applied to the faults over 20–0 Ma in the preferred model represent out-of-sequence deformation relative to the period of deformation interpreted from thermochronology and geologic constraints. Apatite fission track cooling ages from the region indicate the time at which the rocks were exhumed to  $\sim 110 \pm 10$  °C (Gallagher et al., 1998). As a result, later phases of deformation may not be resolved well, especially if the structures in question were not sampled in detail, or accompanied by significant exhumation. The geologic constraints that led us to terminate EC deformation (Gillis et al., 2006; Horton, 2005) do not strictly prohibit localized deformation in the vicinity of the RNF or CF. Modern seismicity indicates that both faults continue to accommodate strike-slip displacements on nearly vertical fault planes (Fig. 6), but the available focal mechanisms do not indicate active thrust faulting (Dewey and Lamb, 1992; Funning et al., 2005). From 5 to 0 Ma in the preferred model, the CF and RNF accommodate 5–10 km of fault-parallel slip, but negligible strike-normal shortening (<5 km; see 5 Ma time step in Figs. 10 and 12), consistent with modern seismicity.

### Map-View Shortening Implications

Both the maximum rotation and preferred reconstructions demonstrate that out-of-plane displacements are critical to obtaining the most self-consistent reconstruction with the available kinematic constraints. Regional limb rotations and transpression deformation focused at the orocline core have the combined effect of increasing shortening estimates (Pueyo et al., 2004) over previously published 2-D plane-strain estimates alone (e.g., Müller et al., 2002; McQuarrie, 2002). The preferred model estimates  $\sim 340$  km of shortening at the orocline axis, compared to  $\sim 270$  km estimated by cross section alone (Eichelberger et al., 2013). The  $\sim 70$  km of additional map-view shortening at the core is due to the combined effect of transpression shortening ( $\sim 50$  km) at the RNF and  $\sim 20$  km of additional SA shortening due to the imposed curved slip paths from limb rotation. Including Altiplano shortening ( $\sim 40$  km; McQuarrie, 2002) and the shortening estimate error at the orocline axis ( $\sim 15\%$ ; Eichelberger et al., 2013), total map-view shortening at the orocline axis would be  $380 \pm 50$  km. Total map-view shortening for both orocline limbs is also higher compared to published plane-strain estimates (Fig. 14). For the northern limb, the preferred model predicts  $\sim 370$  km compared to  $\sim 280$ – $300$  km (McQuarrie, 2002; McQuarrie et al., 2008). There, the 70–90 km increase is due to  $\sim 20$  km of additional SA shortening imposed by rotation and  $\sim 60$ – $70$  km of transpression shortening along the CF (Table 2). In the southern limb the preferred model predicts  $\sim 300$ – $350$  km of shortening compared to  $\sim 280$ – $330$  km (Dunn et al., 1995; Kley, 1996; McQuarrie, 2002; Müller et al., 2002). The  $\sim 20$  km increase in southern limb shortening is related to SA rotation because RNF offset is negligible in the preferred model.

Shortening rate ranges predicted by the models are 5–10 mm yr<sup>-1</sup> in the EC, 2–4 mm yr<sup>-1</sup> in the northern and central IA, 6–10 mm yr<sup>-1</sup> in the southern IA, and 5–9 mm yr<sup>-1</sup> in the SA (Table 3). The predicted shortening rate during EC deformation (ca. 50–20 Ma) are consistent with rates calculated from balanced cross sections (Barnes et al., 2008; McQuarrie et al., 2008) but are at the upper end the 0–8 mm yr<sup>-1</sup> rate proposed for early ca. 45–30 Ma EC deformation in southernmost Bolivia (Oncken et al., 2006) (transect 5, Fig. 4A). SA shortening rates from 15 to 0 Ma in the models are also similar to cross-section shortening rates, but lower than the 9–16 mm yr<sup>-1</sup> SA rates from 10 to 0 Ma proposed by Oncken et al. (2006). Although the modeled shortening rates do not consider short-term (<5 m.y.) fluctuations, the modeled 5–9

mm yr<sup>-1</sup> SA rate is more consistent with Quaternary shortening rates of 7–10 mm yr<sup>-1</sup> (Echavarría et al., 2003; Uba et al., 2009). The maximum rotation and preferred models impose limb rotations similar to GPS data (Allmendinger et al., 2005) and predict average SA shortening rates of 6–9 mm yr<sup>-1</sup>, at the low end of 9–13 mm yr<sup>-1</sup> GPS rates from the southern SA (Brooks et al., 2011).

In the minimum rotation model SA shortening is 5–10 km greater than cross-section estimates and 20–25 km greater in the maximum rotation and preferred models (Table 2). At face value, the preferred model estimates increase the SA shortening differential between southern Peru to the orocline axis to 88 km (based on 17 km of SA shortening; Gotberg et al., 2010), corresponding to  $\sim 6^\circ$  rotation for the northern limb. Between the axis and northern Argentina, the predicted differential is 45 km (60 km of SA shortening; Echavarría et al., 2003), corresponding to  $\sim 5^\circ$  of rotation. In both cases, this represents slightly less than half the total rotation imposed in the model ( $\sim 13^\circ$ ). If curved SA slip paths accommodated limb rotation as modeled, regional bending unassociated with shortening may be partially responsible for modern orogenic curvature. Alternatively, if SA cross-section shortening estimates represent the total SA displacement field, only  $\sim 3^\circ$ – $5^\circ$  of rotation can be attributed to an SA shortening gradient (Eichelberger et al., 2013), while the remaining  $8^\circ$ – $10^\circ$  would be related to regional bending. Ultimately, the models indicate that  $\sim 13^\circ$  of limb rotation produces the most kinematically viable reconstructions, but the relative rotational contributions of differential shortening, curved slip paths, and regional bending are uncertain.

At the orocline axis, predicted map-view shortening from the preferred model is equivalent, within error, to the 400 km shortening estimate modeled by restoring the central Andean rotation pattern paleomagnetic data (Arriagada et al., 2008) (Fig. 14). Both rotationally modeled and plane-strain shortening estimates have been used to estimate crustal thickness based on cross-section area (e.g., Gotberg et al., 2010; Kley and Monaldi, 1998; McQuarrie, 2002). The reconstructions presented here suggest that the out-of-plane contribution to shortening may be as high as  $\sim 90$  km. The map-view shortening estimates for both limbs and the orocline axis exceed the magnitude required to account for the modern cross-sectional area (Fig. 14) without requiring significant additional shortening in the forearc. As a result, shortening at the orocline may be sufficient to account for, and even exceed, modern crustal thickness. From a crustal budget perspective, this opens the possibility that crustal material may have been transferred by lower

*Bolivian orocline reconstruction*

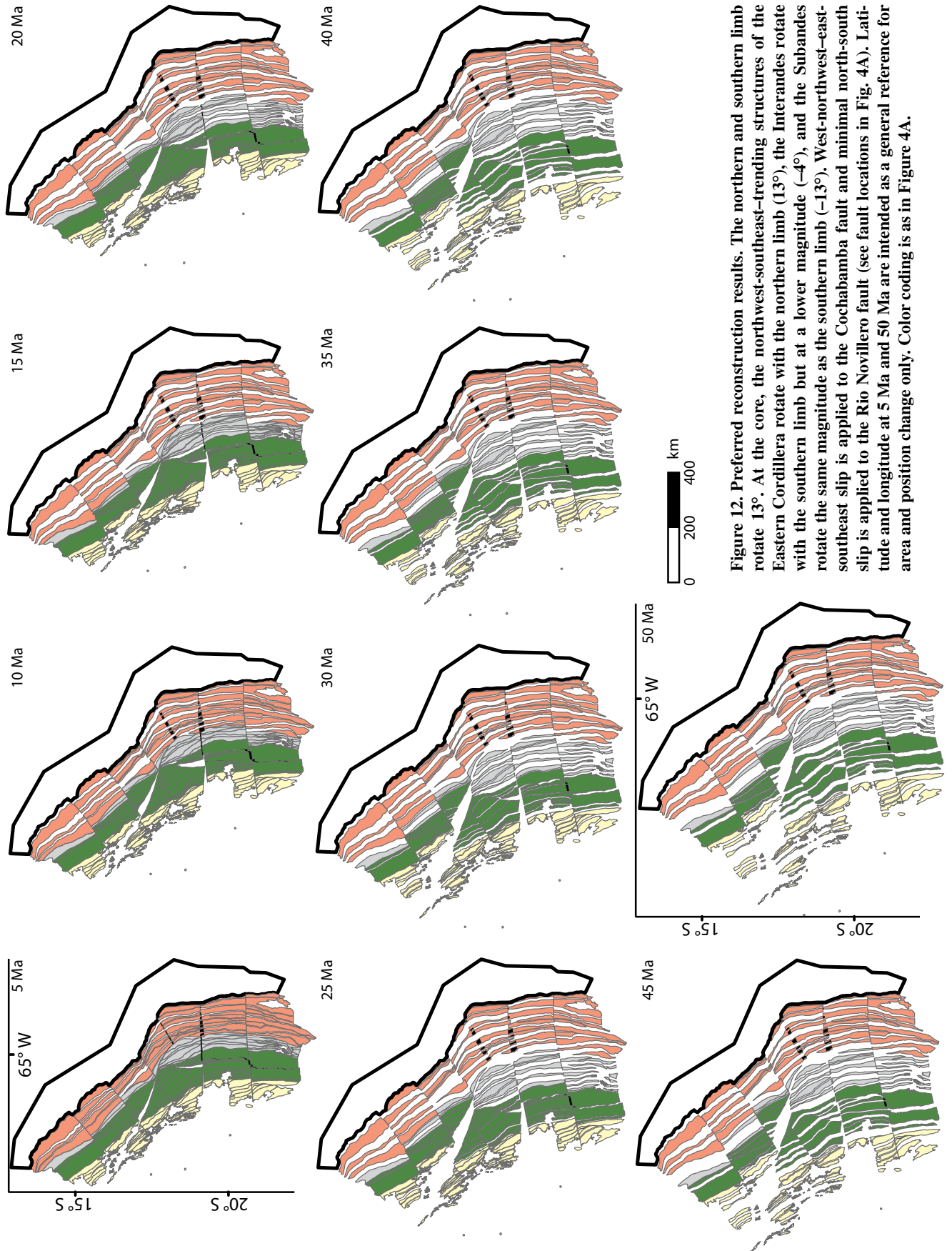


Figure 12. Preferred reconstruction results. The northern and southern limb rotate 13°. At the core, the northwest-southeast-trending structures of the Eastern Cordillera rotate with the northern limb (13°), the Interandes rotate with the southern limb but at a lower magnitude (–4°), and the Subandes rotate the same magnitude as the southern limb (–13°). West-northwest–east-southeast slip is applied to the Cochabamba fault and minimal north-south slip is applied to the Rio Novillero fault (see fault locations in Fig. 4A). Latitude and longitude at 5 Ma and 50 Ma are intended as a general reference for area and position change only. Color coding is as in Figure 4A.

Figure 13. Plot of overlap area at each time step for the preferred model. Symbols and shading as in Figure 8.

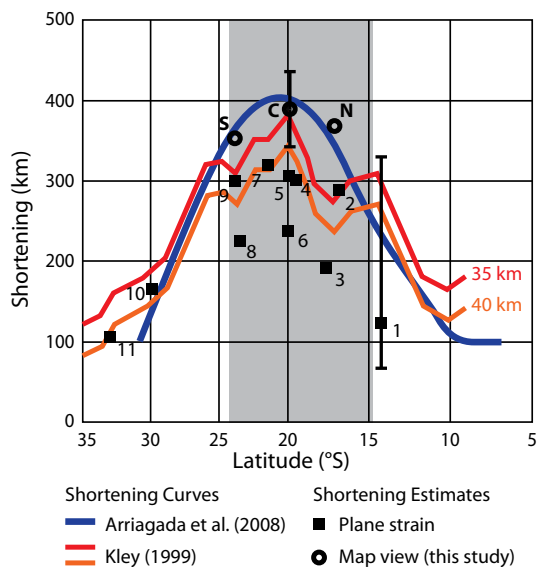
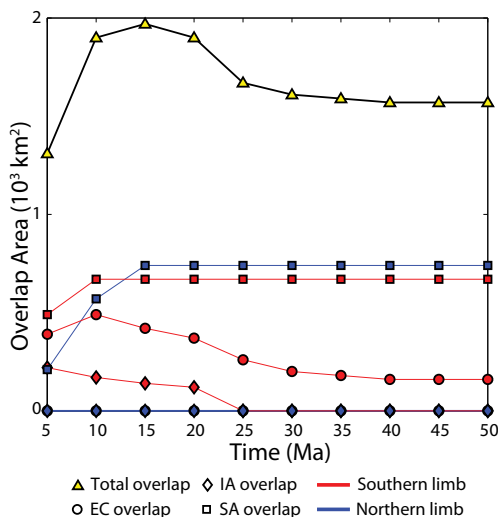


Figure 14. Plot of variation in crustal shortening estimates along the strike at the Bolivian orocline. The latitudes covered by the reconstructions are shaded gray. Plane-strain shortening estimates based on balanced cross sections are plotted as black squares (modified from Gotberg et al., 2010). Shortening estimated from map-view restoration paths in the preferred model are plotted as hollow circles for the southern limb (S), orocline core (C), and northern limb (N). Uncertainties in these estimates are also plotted where available. Crustal area curves for initial crustal thicknesses of 35–40 km are plotted in red and orange (modified from Kley, 1999). The heavy blue curve represents the distribution of shortening required to restore the central Andean rotation pattern paleomagnetic data (modified from Arriagada et al., 2008). Referenced shortening estimates: 1—Gotberg et al. (2010); 2—McQuarrie et al. (2008); 3—Baby et al. (1997); 4—McQuarrie (2002); 5—Eichelberger et al. (2013); 6—Sheffels (1990), Lamb and Hoke (1997); 7—McQuarrie (2002); 8—Baby et al. (1997), Dunn et al. (1995), Kley (1996); 9—Kley (1996), Müller et al. (2002), Elger et al. (2005); 10—Grier et al. (1991), Coutand et al. (2001); 11—Allmendinger et al. (1990), Zapata and Allmendinger (1996).

TABLE 3. MODEL SHORTENING RATES

Transect	Model timing (Ma)	Duration (m.y.)	Minimum rotation (mm yr <sup>-1</sup> )	Maximum rotation (mm yr <sup>-1</sup> )	Preferred (mm yr <sup>-1</sup> )
<b>Eastern Cordillera</b>					
1a	50–25	25	5	5	7
1b	50–25	25	5	5	8
2	50–25	25	6	6	8
3	50–25	25	5	6	6
4	40–20	20	10	7	6
5	40–20	20	8	6	5
<b>Interandes</b>					
1a	45–25	20	2	3	3
1b	45–25	20	2	3	3
2	20–10	10	4	4	4
3	45–15	30	2	2	3
4	25–15	10	9	10	10
5	20–10	10	7	6	6
<b>Subandes</b>					
1a	15–0	15	5	6	6
1b	15–0	15	5	6	6
2	10–0	10	8	9	9
3	15–0	15	6	7	7
4	15–0	15	5	6	6
5	15–0	15	6	7	7



*Bolivian orocline reconstruction*

crustal flow or removed entirely via delamination events. Enhanced lithospheric thickening related to orocline formation has been linked to delamination in the Cantabrian orocline of northern Iberia (Gutiérrez-Alonso et al., 2004).

**CONCLUSIONS**

The map-view reconstructions presented here integrate plane-strain shortening estimates, structural orientations, paleomagnetic rotations, and deformation timing constraints from thermochronology and geology into 3-D kinematic models for the Bolivian orocline. These models indicate that material displacements parallel to orogenic trend are critical to produce kinematically viable orocline reconstructions. In particular, out-of-plane displacements are largely the result of convergent orocline limb rotations that are accommodated at the orocline core by strike-slip and transpressional faulting. Overall, the reconstructed displacement field suggests that map-view shortening estimates may account for, or even exceed, modern crustal thickness at the central Andes. In general, plane-strain studies of deformation (such as balanced cross sections) in areas of orogenic curvature only record a portion of the total orogenic displacement field. Here, map-view shortening estimates from the reconstruction may exceed those required to account for modern crustal thicknesses. If correct, this suggests that formation of the Bolivian orocline contributed to localized crustal thickening and lower crustal loss proposed to explain rapid surface uplift in the Altiplano.

Our main conclusions are as follows.

1. By accounting for limb rotation, kinematic compatibility as measured by map-view overlap was drastically improved over a reconstruction with no rotation (plane-strain model). North-south displacements on the strike-slip RNF further reduced kinematic incompatibilities at the orocline core. Final overlap in the plane-strain reconstruction was ~14,000 km<sup>2</sup> compared to ~5000 km<sup>2</sup> in the minimum rotation model (6°), and ~3000 km<sup>2</sup> in the maximum rotation model (13°). The minimum rotation model predicted ~90 km of strike-slip displacement on the RNF fault while the maximum rotation model predicted ~45 km of slip.

2. We developed a third, preferred model based on the maximum rotation model. The preferred model includes minor rotations at the orocline core and slip on both the RNF and CF, resulting in ~1600 km<sup>2</sup> of final overlap. This model applied ~50 km of left-lateral slip on the CF and <10 km of slip on the RNF. Imposed transpressional deformation predicted ~60–70 km of additional strike-normal shortening in the vicinity of the CF and ~50 km of shortening

near the RNF. The model predicts that some of this shortening occurs after the main phase of deformation in the EC (before 25 Ma) where the faults are located.

3. In the preferred model, the combined effect of limb rotation and transpressional deformation produces map-view shortening estimates that are greater than in cross-section shortening estimates. Map-view shortening predicted by the preferred model is ~370 km in the northern limb, ~380 km at the orocline core, and 320–340 km in the southern limb. Lower shortening estimates are predicted for the southern limb because transpressional shortening is limited to the orocline core and northern limb. The 70–90 km increase in shortening in the northern limb and orocline core is the result of 60–70 km of transpressional shortening and ~20 km of additional SA shortening due to curved slip paths.

4. Increases in SA shortening due to the curved slip paths imposed in the model would result in 5°–6° of limb rotation due to differential shortening between southern Peru, the orocline core, and northern Argentina. This is slightly less than half the total rotation applied in the preferred model, suggesting that regional bending may be a factor. If limb rotation is not the result of curved slip as modeled here, 8°–10° of the total 13° limb rotations required for kinematic compatibility would have to be the result of regional bending.

5. Map-view shortening at the orocline axis is predicted to be 380 ± 50 km. This value exceeds the magnitude required to account for modern cross-section area of the crust. This suggests that deformation at the orocline may be sufficient to account for the modern crustal thickness without significant additional shortening in the forearc. This opens the possibility that any excess may have been transferred along strike by lower crustal flow or removed from the system entirely by processes such as delamination.

**ACKNOWLEDGMENTS**

We thank Stephen Johnston and an anonymous reviewer for their feedback and insightful comments on the initial version of this paper. Early versions of the reconstructions benefitted from discussions with Carmala Garzzone, Laura Wagner, Todd Ehlers, Susan Beck, George Zandt, Brian Horton, Chris Poulsen, and their respective students. These interactions took place at workshops organized as part of the Central Andean Geodynamics and High Topography (CAUGHT) project funded by the National Science Foundation (NSF grant EAR-0908972 to McQuarrie). Blair Schoene provided comments on an early version of the manuscript. Melissa Brenneman created the original ArcGIS (geographic information system) script that produced the reconstructions shown here.

**REFERENCES CITED**

- Allmendinger, R.W., Figueroa, D., Snyder, D.B., Beer, J., Mpodozis, C., and Isacks, B.L., 1990, Foreland shortening and crustal balancing in the Andes at 30°S latitude: *Tectonics*, v. 9, p. 789–809, doi:10.1029/TC009i004p00789.
- Allmendinger, R.W., Smalley, R., Jr., Bevis, M., Caprio, H., and Brooks, B., 2005, Bending the Bolivian orocline in real time: *Geology*, v. 33, p. 905–908, doi:10.1130/G21779.1.
- Arriagada, C., Roperch, P., Mpodozis, C., and Fernandez, R., 2006, Paleomagnetism and tectonics of the southern Atacama Desert (25–28°S), northern Chile: *Tectonics*, v. 25, TC4001, doi:10.1029/2005TC001923.
- Arriagada, C., Roperch, P., Mpodozis, C., and Cobbold, P.R., 2008, Paleogene building of the Bolivian Orocline; tectonic restoration of the central Andes in 2-D map view: *Tectonics*, v. 27, TC6014, doi:10.1029/2008TC002269.
- Baby, P., Herail, G., Salinas, R., and Sempere, T., 1992, Geometry and kinematic evolution of passive roof duplexes deduced from cross section balancing: Example from the foreland thrust system of the southern Bolivian Subandean Zone: *Tectonics*, v. 11, p. 523–536, doi:10.1029/91TC03090.
- Baby, P., Rochat, P., Mascle, G., and Herail, G., 1997, Neogene shortening contribution to crustal thickening in the backarc of the Central Andes: *Geology*, v. 25, p. 883–886, doi:10.1130/0091-7613(1997)025<0883: NSCTCT>2.3.CO;2.
- Barke, R., Lamb, S.H., and MacNiocaill, C., 2007, Late Cenozoic bending of the Bolivian Andes; new paleomagnetic and kinematic constraints: *Journal of Geophysical Research*, v. 112, B01101, doi:10.1029/2006JB004372.
- Barnes, J.B., and Ehlers, T.A., 2009, End member models for Andean Plateau uplift: *Earth-Science Reviews*, v. 97, p. 105–132, doi:10.1016/j.earscirev.2009.08.003.
- Barnes, J.B., and Heins, W.A., 2009, Plio-Quaternary sediment budget between thrust belt erosion and foreland deposition in the central Andes, southern Bolivia: *Basin Research*, v. 21, p. 91–109, doi:10.1111/j.1365-2117.2008.00372.x.
- Barnes, J.B., Ehlers, T.A., McQuarrie, N., O'Sullivan, P.B., and Pelletier, J.D., 2006, Eocene to recent variations in erosion across the central Andean fold-thrust belt, northern Bolivia; implications for plateau evolution: *Earth and Planetary Science Letters*, v. 248, p. 118–133, doi:10.1016/j.epsl.2006.05.018.
- Barnes, J.B., Ehlers, T.A., McQuarrie, N., O'Sullivan, P.B., and Tawakkoli, P.B., 2008, Thermochronometer record of central Andean Plateau growth, Bolivia (19.5° S): *Tectonics*, v. 27, TC3003, doi:10.1029/2007TC002174.
- Barnes, J.B., Ehlers, T.A., Insel, N., McQuarrie, N., and Poulsen, C.J., 2012, Linking orography, climate, and exhumation across the central Andes: *Geology*, v. 40, p. 1135–1138, doi:10.1130/G33229.1.
- Brooks, B.A., and 12 others, 2011, Orogenic-wedge deformation and potential for great earthquakes in the central Andean backarc: *Nature Geoscience*, v. 4, p. 380–383, doi:10.1038/ngeo1143.
- Carey, S.W., 1955, The orocline concept in geotectonics, part I: *Royal Society of Tasmania Papers and Proceedings*, v. 89, p. 255–288.
- Coutand, I., Gautier, P., Cobbold, P.R., de Urreiztieta, M., Chauvin, A., Gapais, D., Rossello, E.A., and Lopez-Gammundi, O., 2001, Style and history of Andean deformation, Puna Plateau, northwestern Argentina: *Tectonics*, v. 20, p. 210–234, doi:10.1029/2000TC900031.
- Dahlstrom, C.D.A., 1969, Balanced cross sections: *Canadian Journal of Earth Sciences*, v. 6, p. 743–757, doi:10.1139/e69-069.
- DeCelles, P.G., and Horton, B.K., 2003, Early to middle Tertiary foreland basin development and the history of Andean crustal shortening in Bolivia: *Geological Society of America Bulletin*, v. 115, p. 58–77, doi:10.1130/0016-7606(2003)115<0058:ETMTFB>2.0.CO;2.
- Dewey, J.F., and Lamb, S.H., 1992, Active tectonics of the Andes, in Oliver, R.A., et al., eds., *Andean geodynamics: Tectonophysics*, v. 205, p. 79–95, doi:10.1016/0040-1951(92)90419-7.

- Dunn, J.F., Hartshorn, K.G., and Hartshorn, P.W., 1995, Structural styles and hydrocarbon potential of the Subandean thrust belt of southern Bolivia, *in* Tankard, A.J., et al., eds., *Petroleum basins of South America: American Association of Petroleum Geologists Memoir 62*, p. 523–543.
- Echavarría, L., Hernández, R., Allmendinger, R., and Reynolds, J., 2003, Subandean thrust and fold belt of northwestern Argentina: Geometry and timing of the Andean evolution: *American Association of Petroleum Geologists Bulletin*, v. 87, p. 965–985, doi:10.1306/01200300196.
- Ege, H., Sobel, E.R., Scheuber, E., and Jacobshagen, V., 2007, Exhumation history of the southern Altiplano plateau (southern Bolivia) constrained by apatite fission-track thermochronology: *Tectonics*, v. 26, TC1004, doi:10.1029/2005TC001869.
- Eichelberger, N., and McQuarrie, N., 2015, Three-dimensional (3-D) finite strain at the central Andean orocline and implications for grain-scale shortening in orogens: *Geological Society of America Bulletin*, v. 127, p. 87–112, doi:10.1130/B30968.1.
- Eichelberger, N., McQuarrie, N., Ehlers, T.A., Enkelmann, E., Barnes, J.B., and Lease, R.O., 2013, New constraints on the chronology, magnitude, and distribution of deformation within the central Andean orocline: *Tectonics*, v. 32, p. 1432–1453, doi:10.1002/tect.20073.
- Elger, K., Oncken, O., and Glodny, J., 2005, Plateau-style accumulation of deformation; southern Altiplano: *Tectonics*, v. 24, TC4020, doi:10.1029/2004TC001675.
- Funning, G.J., Barke, R.M.D., Lamb, S.H., Minaya, E., Parsons, B., and Wright, T.J., 2005, The 1998 Aiquile, Bolivia earthquake: A seismically active fault revealed with InSAR: *Earth and Planetary Science Letters*, v. 232, p. 39–49, doi:10.1016/j.epsl.2005.01.013.
- Gallagher, K., Brown, R., and Johnson, C., 1998, Fission track analysis and its applications to geological problems: *Annual Reviews in Earth and Planetary Science*, v. 26, p. 519–572, doi:10.1146/annurev.earth.26.1.519.
- Garzzone, C.N., Hoke, G.D., Libarkin, J.C., Withers, S., MacFadden, B., Eiler, J., Ghosh, P., and Mulch, A., 2008, Rise of the Andes: *Science*, v. 320, p. 1304–1307, doi:10.1126/science.1148615.
- Gillis, R.J., Horton, B.K., and Grove, M., 2006, Thermochronology, geochronology, and upper crustal structure of the Cordillera Real: Implications for Cenozoic exhumation of the Central Andean Plateau: *Tectonics*, v. 25, TC6007, doi:10.1029/2005TC001887.
- Gotberg, N., McQuarrie, N., and Caillaux, V.C., 2010, Comparison of crustal thickening budget and shortening estimates in southern Peru (12–14°S): Implications for mass balance and rotations in the “Bolivian orocline”: *Geological Society of America Bulletin*, v. 122, p. 727–742, doi:10.1130/B26477.1.
- Gregory-Wodzicki, K.M., 2000, Relationships between leaf morphology and climate, Bolivia: Implications for estimating paleoclimate from fossil floras: *Paleobiology*, v. 26, p. 668–688, doi:10.1666/0094-8373(2000)026<0668:RBLMAC>2.0.CO;2.
- Grier, M.E., Salfity, J.A., and Allmendinger, R.W., 1991, Andean reactivation of the Cretaceous Salta rift, northwestern Argentina: *Journal of South American Earth Sciences*, v. 4, p. 351–372, doi:10.1016/0895-9811(91)90007-8.
- Gutiérrez-Alonso, G., Fernández-Suárez, J., and Weil, A.B., 2004, Orocline triggered lithospheric delamination, *in* Sussman, A.J., and Weil, A.B., eds., *Orogenic curvature: Integrating paleomagnetic and structural analyses: Geological Society of America Special Paper 383*, p. 121–131, doi:10.1130/0-8137-2383-3(2004) 383 [121:OTLD] 2.0.CO;2.
- Gutiérrez-Alonso, G., Murphy, B., Fernández-Suárez, J., Weil, A.B., Franco, M.P., and Gonzalo, J.C., 2011, Lithospheric delamination in the core of Pangea: Sm–Nd insights from the Iberian mantle: *Geology*, v. 39, p. 155–158, doi:10.1130/G31468.1.
- Hindle, H., and Burkhard, M., 1999, Strain, displacement and rotation associated with the formation of curvature on fold belts: The example of the Jura arc: *Journal of Structural Geology*, v. 21, p. 1089–1101, doi:10.1016/S0191-8141(99)00021-8.
- Hindle, D., Kley, J., Oncken, O., and Sobolev, S., 2005, Crustal balance and crustal flux from shortening estimates in the Central Andes: *Earth and Planetary Science Letters*, v. 230, p. 113–124, doi:10.1016/j.epsl.2004.11.004.
- Hoke, G.D., and Garzzone, C.N., 2008, Paleosurfaces, paleoelevation, and the mechanisms for the late Miocene topographic development of the Altiplano plateau: *Earth and Planetary Science Letters*, v. 271, p. 192–201, doi:10.1016/j.epsl.2008.04.008.
- Horton, B.K., 2005, Revised deformation history of the Central Andes: Inferences from Cenozoic foredeep and intermontane basins of the Eastern Cordillera, Bolivia: *Tectonics*, v. 24, TC3011, doi:10.1029/2003TC001619.
- Horton, B.K. and DeCelles, P.G., 1997, The modern foreland basin system adjacent to the Central Andes: *Geology*, v. 25, p. 895–898.
- Isacks, B.L., 1988, Uplift of the Central Andean Plateau and bending of the Bolivian Orocline: *Journal of Geophysical Research*, v. 93, p. 3211–3231, doi:10.1029/JB093iB04p03211.
- Johnston, S.T., Weil, A.B., and Gutiérrez-Alonso, G., 2013, Oroclines: Thick and thin: *Geological Society of America Bulletin*, v. 125, p. 643–663, doi:10.1130/B30765.1.
- Kennan, L., Lamb, S.H., and Rundle, C., 1995, K–Ar dates from the Altiplano and Cordillera Oriental of Bolivia: Implications for Cenozoic stratigraphy and tectonics: *Journal of South American Earth Sciences*, v. 8, p. 163–186, doi:10.1016/0895-9811(95)00003-X.
- Kley, J., 1996, Transition from basement-involved to thin-skinned thrusting in the Cordillera Oriental of southern Bolivia: *Tectonics*, v. 15, p. 763–775, doi:10.1029/95TC03868.
- Kley, J., 1999, Geologic and geometric constraints on a kinematic model of the Bolivian orocline: *Journal of South American Earth Sciences*, v. 12, p. 221–235, doi:10.1016/S0895-9811(99)00015-2.
- Kley, J., and Monaldi, C.R., 1998, Tectonic shortening and crustal thickness in the Central Andes: How good is the correlation?: *Geology*, v. 26, p. 723–726, doi:10.1130/0091-7613(1998)026<0723:TSACTI>2.3.CO;2.
- Lamb, S., and Hoke, L., 1997, Origin of the high plateau in the Central Andes, Bolivia, South America: *Tectonics*, v. 16, p. 623–649, doi:10.1029/97TC00495.
- Laubscher, H.P., 1965, Ein kinematisches Modell der Juraufaltung: *Eclogae Geologicae Helveticae*, v. 58, p. 232–318.
- McQuarrie, N., 2002, The kinematic history of the central Andean fold-thrust belt, Bolivia: Implications for building a high plateau: *Geological Society of America Bulletin*, v. 114, p. 950–963, doi:10.1130/0016-7606(2002)114<0950:TKHOTC>2.0.CO;2.
- McQuarrie, N., and Davis, G.H., 2002, Crossing the several scales of strain-accomplishing mechanisms in the hinterland of the central Andean fold-thrust belt, Bolivia: *Journal of Structural Geology*, v. 24, p. 1587–1602.
- McQuarrie, N., and Wernicke, B.P., 2005, An animated tectonic reconstruction of southwestern North America since 36 Ma: *Geosphere*, v. 1, p. 147–172, doi:10.1130/GES00016.1.
- McQuarrie, N., Horton, B.K., Zandt, G., Beck, S., and DeCelles, P.G., 2005, Lithospheric evolution of the Andean fold-thrust belt, Bolivia, and the origin of the central Andean plateau: *Tectonophysics*, v. 399, p. 15–37, doi:10.1016/j.tecto.2004.12.013.
- McQuarrie, N., Barnes, J.B., and Ehlers, T.A., 2008, Geometric, kinematic, and erosional history of the central Andean Plateau, Bolivia (15–17°S): *Tectonics*, v. 27, TC3007, doi:10.1029/2006TC002054.
- Müller, J.P., Kley, J., and Jacobshagen, V., 2002, Structure and Cenozoic kinematics of the Eastern Cordillera, southern Bolivia: *Tectonics*, v. 21, p. 1–1–24, doi:10.1029/2001TC001340.
- Oncken, O., Hindle, D., Kley, J., Elger, K., Victor, P., and Schemmann, K., 2006, Deformation of the central Andean upper plate system—Facts, fiction, and constraints for plateau models, *in* Oncken, O., et al., eds., *The Andes: Active subduction orogeny*: Berlin, Springer-Verlag, p. 3–27.
- Pardo-Casas, F., and Molnar, P., 1987, Relative motion of the Nazca (Farallon) and South American plates since Late Cretaceous time: *Tectonics*, v. 6, p. 233–248, doi:10.1029/TC006i003p0233.
- Pueyo, E.L., Pocoví, A., Millán, H., and Sussman, A.J., 2004, Map-view models for correcting and calculating shortening estimates in rotated thrust fronts using paleomagnetic data, *in* Sussman, A.J., and Weil, A.B., eds., *Orogenic curvature: Integrating paleomagnetic and structural analyses: Geological Society of America Special Paper 383*, p. 57–71, doi:10.1130/0-8137-2383-3(2004)383[57:MMFAC]2.0.CO;2.
- Roperch, P., Sempere, T., Macedo, O., Arriagada, C., Fornari, M., Tapia, C., García, M., and Laj, C., 2006, Counterclockwise rotation of late Eocene–Oligocene fore-arc deposits in southern Peru and its significance for oroclinal bending in the central Andes: *Tectonics*, v. 25, TC3010, doi:10.1029/2005TC001882.
- Roperch, P., Carlotto, V., Ruffet, G., and Fornari, M., 2011, Tectonic rotations and transcurent deformation south of the Abancay deflection in the Andes of southern Peru: *Tectonics*, v. 30, TC2010, doi:10.1029/2010TC002725.
- Scheuber, E., Mertmann, D., Ege, H., Silva-Gonzalez, P., Heubeck, C., Reutter, K., and Jacobshagen, V., 2006, Exhumation and basin development related to formation of the central Andean Plateau, 21°S, *in* Oncken, O., et al., eds., *The Andes: Active Subduction Orogeny*: Berlin, Germany, Springer, p. 285–301.
- Schmitz, M., and Kley, J., 1997, The geometry of the central Andean backarc crust: Joint interpretation of cross-section balancing and seismic refraction data: *Journal of South American Earth Sciences*, v. 10, p. 90–110.
- Sempere, T., Heraül, G., Oller, J., and Bonhomme, M.G., 1990, Late Oligocene–early Miocene major tectonic crisis and related basins in Bolivia: *Geology*, v. 18, p. 946–949, doi:10.1130/0091-7613(1990)018<0946:LOEMMT>2.3.CO;2.
- Sheffels, B.M., 1988, Structural constraints on structural shortening in the Bolivian Andes [Ph.D. thesis]: Cambridge, Massachusetts Institute of Technology, 167 p.
- Sheffels, B., 1990, Lower bound on the amount of crustal shortening in the central Bolivian Andes: *Geology*, v. 18, p. 812–815, doi:10.1130/0091-7613(1990)018<0812:LBOTAO>2.3.CO;2.
- Sheffels, B.M., 1995, Is the bend in the Bolivian Andes an orocline?, *in* Tankard, A.J., et al., eds., *Petroleum basins of South America: American Association of Petroleum Geologists Memoir 62*, p. 511–522.
- Somoza, R., 1998, Updated Nazca (Farallon)–South America relative motions during the last 40 My: Implications for mountain building in the central Andean region: *Journal of South American Earth Sciences*, v. 11, p. 211–215, doi:10.1016/S0895-9811(98)00012-1.
- Sussman, A.J., Pueyo, E.L., Chase, C.G., Mitra, G., and Weil, A.B., 2012, The impact of vertical-axis rotations on shortening estimates: *Lithosphere*, v. 4, p. 383–394, doi:10.1130/L177.1.
- Wigger, P.J., Schmitz, M., Arana, M., Asch, G., Balducci, S., Giese, P., Heinsdorf, W.-D., Martínez, E., Riccardi, E., Röwer, P., and Viraumont, J., 1994, Variation in the crustal structure of the southern Central Andes deduced from seismic refraction investigations, *in* Reutter, K. J., et al., eds., *Tectonics of the Southern Central Andes: Structure and Evolution of an Active Continental Margin*: Springer, New York, p. 23–48.
- Uba, C.E., Heubeck, C., and Hulka, C., 2005, Facies analysis and basin architecture of the Neogene Subandean synorogenic wedge, southern Bolivia: *Sedimentary Geology*, v. 180, p. 91–123, doi:10.1016/j.sedgeo.2005.06.013.
- Uba, C.E., Heubeck, C., and Hulka, C., 2006, Evolution of the late Cenozoic Chaco foreland basin, southern Bolivia: *Basin Research*, v. 18, p. 145–170, doi:10.1111/j.1365-2117.2006.00291.x.
- Uba, C.E., Kley, J., Strecker, M.R., and Schmitt, A., 2009, Unsteady evolution of the Bolivian Subandean thrust belt: The role of enhanced erosion and clastic wedge progradation: *Earth and Planetary Science Letters*, v. 281, p. 134–146, doi:10.1016/j.epsl.2009.02.010.
- Yonkee, A., and Weil, A.B., 2010, Reconstructing the kinematic evolution of curved mountain belts: Internal strain patterns in the Wyoming salient, Sevier thrust belt, U.S.A.: *Geological Society of America Bulletin*, v. 122, p. 24–49, doi:10.1130/B26484.1.
- Zapata, T.R., and Allmendinger, R.W., 1996, Thrust-front zone of the Precordillera, Argentina: A thick-skinned triangle zone: *American Association of Petroleum Geologists Bulletin*, v. 80, p. 359–381.

# Geosphere

## Kinematic reconstruction of the Bolivian orocline

Nathan Eichelberger and Nadine McQuarrie

*Geosphere* published online 11 March 2015;  
doi: 10.1130/GES01064.1

---

**Email alerting services** click [www.gsapubs.org/cgi/alerts](http://www.gsapubs.org/cgi/alerts) to receive free e-mail alerts when new articles cite this article

**Subscribe** click [www.gsapubs.org/subscriptions/](http://www.gsapubs.org/subscriptions/) to subscribe to Geosphere

**Permission request** click <http://www.geosociety.org/pubs/copyrt.htm#gsa> to contact GSA

Copyright not claimed on content prepared wholly by U.S. government employees within scope of their employment. Individual scientists are hereby granted permission, without fees or further requests to GSA, to use a single figure, a single table, and/or a brief paragraph of text in subsequent works and to make unlimited copies of items in GSA's journals for noncommercial use in classrooms to further education and science. This file may not be posted to any Web site, but authors may post the abstracts only of their articles on their own or their organization's Web site providing the posting includes a reference to the article's full citation. GSA provides this and other forums for the presentation of diverse opinions and positions by scientists worldwide, regardless of their race, citizenship, gender, religion, or political viewpoint. Opinions presented in this publication do not reflect official positions of the Society.

---

### Notes

---

Advance online articles have been peer reviewed and accepted for publication but have not yet appeared in the paper journal (edited, typeset versions may be posted when available prior to final publication). Advance online articles are citable and establish publication priority; they are indexed by GeoRef from initial publication. Citations to Advance online articles must include the digital object identifier (DOIs) and date of initial publication.

---